Univerzita Karlova v Praze

Matematicko-fyzikální fakulta

DIPLOMOVÁ PRÁCE

Miroslav Kuchta

Termální konvekce s volným povrchem v rotujícím ledovém měsíci

Matematický ústav UK

Vedoucí diplomové práce: Doc. RNDr. Ondřej Čadek, CSc.

Studijní program: Matematika

Studijní obor: Matematické modelování ve fyzice a technice

Praha 2011

Prehlasujem, že som svoju diplomovú prácu vypracoval samostatne a výhradne s použitím citovaných prameňov, literatúry a ďalších odborných zdrojov.

Beriem na vedomie, že sa na moju prácu vzťahujú práva a povinnosti vyplývajúce zo zákona č. 121/2000 Sb., autorského zákona v platnom znení, obzvlášť skutočnosť, že Univerzita Karlova v Praze má právo na uzavretie licenčnej zmluvy o užití tejto práce ako školského diela podľa §60 odst. 1 autorského zákona.

V .... dňa ....

Název práce: Termální konvekce s volným povrchem v rotujícím ledovém měsíci

Autor: Miroslav Kuchta

Katedra: Matematický ústav UK

Vedoucí diplomové práce: Doc. RNDr. Ondřej Čadek, CSc., Katedra geofyziky

Abstrakt: Táto práca sa zaoberá modelovaním povrchových deformácií a termálnej konvekcie v rotujúcom ľadovom mesiaci. Systém riadiacich rovníc, ktoré odvodíme z obecných zákonov zachovania, riešime numericky pomocou metódy konečných diferencií na posunutých sieťach. Voľný povrch chápeme ako implicitne popísané rozhranie medzi mesiacom a takmer nehmotným médiom s rádovo menšou viskozitou ako ľad. Vytvoríme numerickú metódu schopnú sledovať deformovaný povrch. Numerickú metódu aplikujeme na príklady s teplotne závislou viskozitou.

Klíčová slova: Stokes-Fourier systém, Voľný povrch, Konečné diferencie

Title: Thermal convection with evolving surface in a rotating icy satellite

Author: Miroslav Kuchta

Department: Mathematical Institute of Charles University

Supervisor: Doc. RNDr. Ondřej Čadek, CSc., Department of Geophysics

Abstract: This thesis is concerned with modeling the surface deformations and thermal convection in a rotating icy satellite. The system of governing equations, that we derive from general balance laws, is solved numerically using the finite-difference method on a staggered grid. Free surface is understood as implicitly described interface between the satellite and an almost massless medium with viscosity orders of magnitude smaller than ice. We design a numerical method capable of tracking the deforming surface. The numerical method is applied to models with temperature-dependent viscosity.

Keywords: Stokes-Fourier system, Free surface, Finite-differences

Contents

Introduction

Computer simulations are used to study various phenomena in geophysics. One of such phenomenon is Iapetus, an icy satellite whose flattened shape is inconsistent with its present-day rotational period and whose surface features an equatorial ridge which is unique in the Solar system. Robuchon et al. (2010) and Castillo-Rogez et al. (2007) explained the flattening as a relict from period with fast rotation that Iapetus preserved by forming a lithosphere strong enough to resist the deformations due to despinning. The origin of ridge, however, remains enigmatic with hypothesis that relate its formation to despinning, volcanic, and tectonic activities all awaiting verification.

A challenge of modeling the ridge formation lies in the time-dependent domain where governing equations are solved. Therefore, numerical method must be used that is capable of tracking the deforming domain. Further, the method should also be robust as high-Rayleigh-number convection was likely to occur in Iapetian mantle.

The aim of this thesis is to design a numerical method for simulation of thermal convection inside a deforming rotating icy satellite and thus create a tool that could be later used to explain the formation of the equatorial ridge on Iapetus.

The thesis consists of five chapters. In Chapter 1 we discuss physical properties of icy satellites. In Chapter 2 we derive governing equations that describe the flow of ice inside the mantle. Our method of tracking the deforming surface is explained in Chapter 3. Numerical method for solving the governing equations on the time-dependent domain is then explained in Chapter 4. Finally, in Chapter 5 the method is subjected to tests.

Chapter 1

Physics of Icy Satellites

In this chapter we give an overview of characteristics of icy satellites. We focus especially on heat sources and rheological properties of water ice. The last section is devoted to Iapetus and its mysteries that inspired our work.

1.1 Introduction

Icy satellites in our Solar system revolve around the giant planets, i.e., Jupiter, Saturn, Uranus and Neptune. The main source of information about satellites' properties are flybys by spacecrafts from missions such as Voyager (Jupiter, Saturn, Uranus, Neptune), Galileo (Jupiter) and Cassini (Saturn). The collected data reveals that the moons have the following characteristics in common.

The shape of satellites can be described as a triaxial ellipsoid that corresponds to a figure of rotating and tidally distorted body in the state of hydrostatic equilibrium. The specifics of shape provide details about the moon's history which is typically guided by the evolution scenario by Multhaup and Spohn (2007): (1) Initial phase after accretion with cold interior and warmer surface. (2) The heat from decay of short-lived/long-lived radioactive isotopes warms the interior from within. (3) Possible onset of convection which cools down warmer interior more effectively than pure conduction. (4) Halt of convection due to exhaustion of heat sources, conductive cooling continues further.

The composition of icy satellites is dominated by water ice, silicates and iron compounds. We will refer to the latter two materials as rock. The density of water ice is $920\,\mathrm{kg.m^{-3}}$. The density of rock can vary between $2500\,\mathrm{kg.m^{-3}}$ for hydrated rock to $8000\,\mathrm{kg.m^{-3}}$ for pure iron (Hussmann et al., 2007). Rock-to-ice fraction can be determined from mean density which is calculated from measuring the satellite's gravitational field assuming that the satellite is homogeneous. No differentiation of the interior is a reasonable starting approximation but the validity of this assumption isn't certain for most of the satellites. A level of differentiation can be expected within the water ice layer of some smaller satellites, as the internal pressures could have been sufficiently large to cause phase transition in ice. The Galilean satellites are predicted to have even complex interiors with iron cores and liquid-water oceans (Spohn and Schubert, 2003).

Existence of liquid layers is related to presence of volatiles (e.g., ammonia) that act as

antifreeze and even in small amounts can significantly reduce the melting point of water ice. Other factors are the heat sources and properties of water ice.

1.2   Heat sources

Accretional heating, radioactive decay and tidal dissipation are the main contributors to heat budget of undifferentiated icy satellite. For differentiated satellite, release of potential energy due to differentiation should also be included among the heat sources.

Accretional energy is especially relevant at the very beginning of the satellite's evolution. It is a fraction h of the kinetic energy of falling planetesimals that is stored underneath the growing surface of satellite. Temperature is therefore higher on the surface than in the interior. The temperature profile $T_a(r)$ for homogeneous accretion is given by Breuer and Moore (2007)

$$T_a\left(r\right) = h\frac{GM_s\left(r\right)}{C_\mathbf{p}r}\left(1 + \frac{ru^2}{2GM_s\left(r\right)}\right) + T_e, \tag{1.2.1}$$

where G is the universal gravitational constant, $M_s(r)$ is the mass of satellite at radial distance r, C_p is the specific heat, u is the average velocity of planetesimals and T_e is the temperature of surrounding nebula.

After the completion of accretion, radiogenic heating becomes the main source of energy. Short-lived radioactive isotopes (SLRI) provide a strong energy peak early in the history while energy from long-lived radioactive isotopes (LLRI) prevails later. The isotopes are contained in the rock component and their initial concentrations C_0^i are determined from the composition of chondrites. The chondrites reflect the state of elemental abundances at the time of formation of the CAIs (Calcium-Aluminum-rich Inclusions) at $4.567\,\mathrm{Gyr}$ (Robuchon et al., 2010). The concentration of i-th isotope $C^i(t)$ decays with time following the law

$$C^i(t) = C_0^i \exp\left(-\frac{\ln 2}{\tau_{1/2}^i}t\right), \tag{1.2.2}$$

where $\tau_{1/2}^i$ is the half-life and t is the time elapsed since the formation of CAIs. The heat production of i-th isotope H^i ($[H^i] = \mathrm{W.kg^{-1}}$) is given by Castillo-Rogez et al. (2009)

$$H^i = \frac{A}{m^i}E_d^i e_v \frac{\ln 2}{\tau_{1/2}^i}, \tag{1.2.3}$$

where A is Avogadro's number, $e_v = 1.60217646 \times 10^{-19}\,\mathrm{J.(eV)^{-1}}$, m^i is the molar weight and E_d^i is the energy per decay of single atom measured in eV. Finally the total volumetric radiogenic heat rate $H_R(t)$ ($[H_R(t)] = \mathrm{W.m^{-3}}$) for the satellite with mean density ρ, rock-to-ice mass ratio χ that contains N isotopes can be calculated as

$$H_R(t) = \rho\chi\sum_{i=1}^{N} H^i C^i(t). \tag{1.2.4}$$

	Element	$\tau_{1/2}^i$(Myr)	C_0^i(ppb)	$H^i(\mu\text{W.kg}^{-1})$
LLRI	^{238}U	4468	26.2	94.65
	^{235}U	703.81	8.2	568.7
	^{232}Th	14.030	53.8	26.38
	^{40}K	1277	1104	29.17
SLRI	^{26}Al	0.716	600	356×10^3
	^{60}Fe	1.5	200	$(68\text{-}74)\times10^3$
	^{53}Mn	3.7	25.7	27×10^3

Table 1.1: Half-lives, initial isotopic abundances and heat productions for important LLRIs and SLRIs. Values adopted from Castillo-Rogez et al. (2007) and van Schmus (1995).

In eq. (1.2.4) $C^i(t)$ is in kg per kg of rock. The properties of important LLRIs and SLRIs are summarized in Table 1.1 where the ordinary chondrites with density $3510\,\text{kg.m}^{-3}$ are considered.

The tidal heating is due to interaction between the satellite and the planet it orbits. The satellite traveling on an elliptical orbit is subjected to gravitational force which varies periodically with the distance from the satellite's primary. If the satellite's interior were elastic, its shape would be instantly rotated in such a way that the tidal bulge would be aligned with the force. In case of viscoelastic interior, the response is not instantaneous and a misalignment of the tidal bulge with respect to the planet causes a torque which slows down rotation of the satellite. The dissipated energy is then the source of tidal heating. The torque M on a satellite in a circular orbit with constant semi-major axis D is given by Peale (1999)

$$M = \frac{3}{2}\frac{k_2\left(t\right)GM_p^2 a\left(t\right)^5}{D^6 Q\left(t\right)}, \tag{1.2.5}$$

where M_p is the mass of the planet, a is the equatorial radius of satellite, k_2 is the second-degree potential Love number and Q^{-1} is the specific dissipation function. The last two quantities depend strongly on rheology; the former describes viscoelastic response of the satellite to external periodic forcing on timescale of the orbital period (Hussmann et al., 2007) while the later corresponds to the ratio between energy dissipated over one cycle and peak energy reached during the tidal cycle (Robuchon et al., 2010). From eq. (1.2.5) time rate of the spin rate w can be calculated following Robuchon et al. (2010) as

$$\frac{d\omega}{dt} = \frac{3}{2}\frac{k_2\left(t\right)GM_p^2 a\left(t\right)^5}{D^6 Q\left(t\right)C\left(t\right)}, \tag{1.2.6}$$

where C is the polar moment of inertia. The lag of the tidal wave, and therefore the torque, is bigger for fast rotating satellites that haven't yet despun into the state of synchronous rotation. In this phase tidal heating is very efficient and can release more energy than the decay of radioactive elements (Breuer and Moore, 2007). The heating continues after the despinning and as the heat rate given by Segatz et al. (1988) suggests, it is most effective

for large satellites on eccentric orbits that are close to the primary

$$H_T = -\frac{21}{2}\frac{a^5 n^5 e^2}{G}\Im\left(k_2\right).$$

(1.2.7)

In eq. (1.2.7), e and n $\left(= \sqrt{G\frac{(M_s+M_p)}{D^3}}\right)$ are the eccentricity and the mean motion, respectively. The last equation hints the link between orbital and thermal evolution of the satellite. The thermal state effects rheology which is related to k_2. The Love number k_2 is related to tidal heating via the aforementioned relation and closing the loop, tidal friction implies loss of orbital energy, i.e., decrease of eccentricity.

1.3   Rheological properties of water ice

Water ice is the major constituent of icy satellites. Understanding its rheological properties is therefore a key to understanding processes in the satellites' interior and their evolution. While there is plenty of laboratory measurements from glaciers, conditions in which extraterrestrial ice exists are too different (e.g., lower temperatures, higher pressures and velocities) to allow just a simple extrapolation of terrestrial data. In the following section we give an overview of the recent knowledge about planetary ice based on (Greve, 2009), (Durham and Stern, 2001).

Water ice is a polycrystalline material. The phase diagram (Fig. 1.1(a)) shows eight types of water ice that are referred to as ice I through VIII. They differ in density, melting temperature, deformation mechanisms, etc. The phase diagram also shows that ices I, III, V, VI, VII can undergo two types of direct transformations: (i) If the temperature profile intersects the melting curve a phase transition could take place and a liquid layer could form an ocean inside the satellite. (ii) Transformation into a different type of ice, which leads to differentiation of the interior.

Laboratory experiments have established the following complicated relation for viscosity of water ice

$$\eta = \frac{1}{2}\delta^{-1+1/n}d^{p/n}\left[A\exp\left(-\frac{E^* + PV^*}{RT}\right)\right]^{-1/n},$$

(1.3.1)

where P is hydrostatic pressure, d is grain size, T is temperature, R is the gas constant and δ is the second invariant of the strain rate tensor $\dot{\boldsymbol{\epsilon}}$ ($\dot{\boldsymbol{\epsilon}}$ is defined as a symmetric part of the velocity gradient). The constants A, activation energy E^*, activation volume V^*, stress exponent n and grain-size exponent p then characterize each mechanism of deformation. To account for whole range of conditions multiple sets of constants might be needed to capture a particular mechanism. Table 1.2 shows that in order to characterize dislocation creep and grain-size-sensitive creep (GSS) of ice I, three and two sets respectively are required.

Mechanisms can operate in an independent or dependent way. In the first case, the effective viscosity of deformation consisting of these mechanisms is calculated as the sum
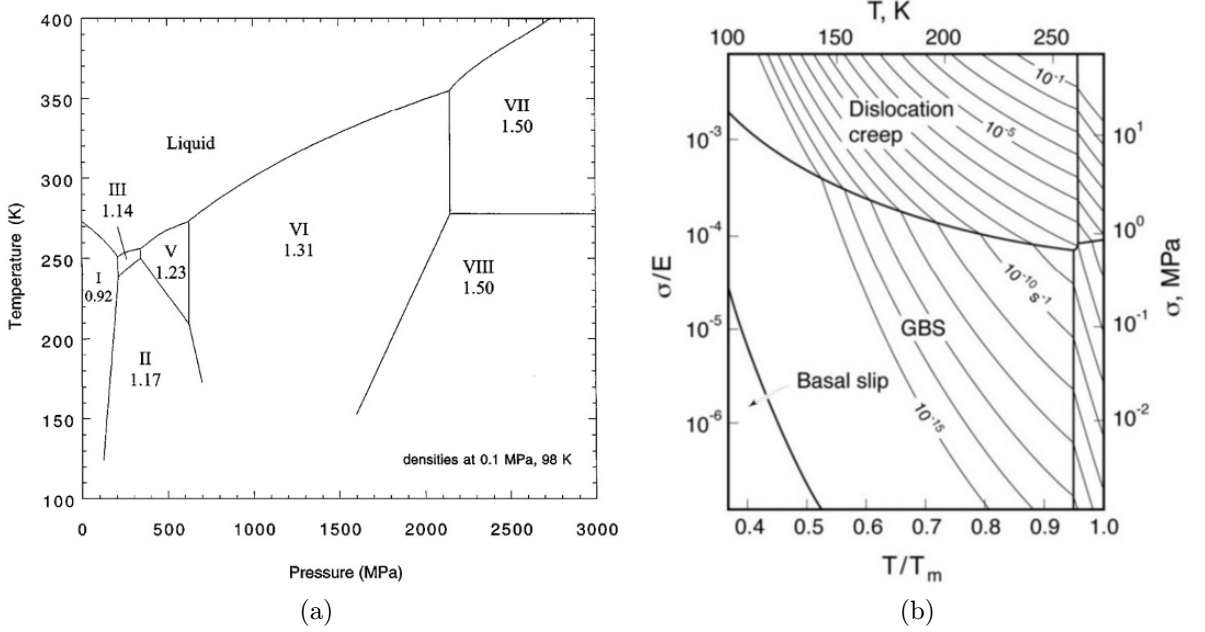
Figure 1.1: Phase diagram and deformation map of water ice. (a) Phase diagram of water ice. (b) Deformation map for ice I. Pressure and grain size are constant, $T_m = 273\,\mathrm{K}$ is the melting temperature, $E = 9.3\,\mathrm{GPa}$ is the Young modulus. Dislocation creep is paired as independent with GSS and basal slip. The former two are combined as dependent. The weaker lines are contours of constant strain rate. Graphs courtesy (Durham and Stern, 2001).

of individual viscosities η_i. In the second case, the effective viscosity is given by

$$\frac{1}{\eta_{tot}} = \sum_i \frac{1}{\eta_i}. \qquad (1.3.2)$$

Table 1.2 shows high stress dependence of all deformation mechanisms of all types of ices. Consequently, using the definition of viscosity in eq. (1.3.1), we can see that a relation between deviatoric part of the stress tensor and strain rate tensor $\boldsymbol{\sigma} = 2\eta\dot{\boldsymbol{\epsilon}}$ is not linear. Thus, by definition water ice is not a Newtonian fluid. We discuss models of non-Newtonian fluids that were used in previous investigations of icy satellites in Section 1.4.

In certain applications, simplified linearized rheology can be used. Water ice can be approximated as a Newtonian fluid by setting $n=1$ in eq. (1.3.1). Moreover, if the grain-size dependence is negligible, p can be set to zero and viscosity then follows the Arrhenius law

$$\eta(T, \rho) = \eta_0 \exp\left(\frac{E^* + PV^*}{RT}\right), \qquad (1.3.3)$$

where η_0 is the reference viscosity and ρ is density. Further, if incompressibility is assumed, the density is constant and the viscosity becomes only a function of temperature. This simplification suppresses all other dependencies but leaves a very important feature of

Creep Regime	$\log A$ $(\mathrm{MPa^{-n}m^{p}s^{-1}})$	p	n	E^* (kJ/mole)	V^* (cm^3/mole)
Dislocation creep					
$T > 258\,\mathrm{K}$	28.8	0	4	181	-13^*
A $T \in (240\,\mathrm{K}, 258\,\mathrm{K})$	11.8 ± 0.4	0	4.0 ± 0.6	91 ± 2	-13^*
B $T \in (?\,\mathrm{K}, 240\,\mathrm{K})$	5.1 ± 0.03	0	4.0 ± 0.1	61 ± 2	-13 ± 3
C $T <?\,\mathrm{K}$	-3.8	0	6.0 ± 0.4	39 ± 5	-13^*
GSS					
$T > 255\,K$	26.5	1.4	1.8	192	-13^*
$T < 255\,K$	-2.4	1.4	1.8	49	-13^*
Basal slip					
	7.74	0	2.4	60	-13^*

Table 1.2: Rheological constants of mechanisms of deformation of ice I. (*) by the value means that the value is estimated not measured. (?) indicates that boundary between Regimes B and C depends on strain rate and temperature. Data from (Durham and Stern, 2001)

rheology; viscosity can act as a thermostat. Following eq. (1.3.3), an increase in temperature will decrease viscosity which encourages convection and thus more effective cooling of the interior.

We conclude this section by stating a simplified constitutive relation for water ice. If modeled as an incompressible, Newtonian fluid with temperature-dependent viscosity, the response of water ice to deformation is given by stress tensor $\boldsymbol{T}$,

$$\boldsymbol{T} = -\pi\mathbb{I} + 2\eta(T)\dot{\boldsymbol{\epsilon}}, \tag{1.3.4}$$

where π is pressure.

1.4   Rheological models

We showed in previous sections that water ice is a non-Newtonian fluid and that its viscoelastic character is necessary for the despinning. In eq. (1.2.6), the time derivative of angular velocity is a function of the second-degree potential Love number; a real part of the complex Love number k_2^c which is computed from rheological profile. The rheological profile, characterized by complex shear modulus μ^c, varies with the frequency of forcing $s = 2\,(\omega - n)$. The forcing frequencies can cover wide interval as the differences between the initial and current spin rates of the icy satellites can be significant (e.g., ~2.10^{-4} Hz for Iapetus rotating with period of 9 hours to ~9.10^{-7} Hz for the spin period of 80 days). There is no experimental data about viscoelastic behavior of ice mixtures at such low frequencies of loading in terrestrial conditions, let alone the conditions on Iapetus and other icy satellites. Therefore, rheological models of viscoelastic fluids have to be used

to predict the response. We will describe two models that were used in calculations that explained the flattening of Iapetus.

1.4.1   Maxwell material

The simplest linear viscoelastic material is the Maxwell material. It was utilized by Castillo-Rogez et al. (2007) in their model with conductive heat transfer. Its model consists of a spring and a dashpot joined in the series. Deformation of the spring is elastic and follows Hooke's law

$$F = \mu\Delta, \tag{1.4.1}$$

where F, Δ and μ are shear stress, shear deformation and shear modulus. Deformation of the dashpot is viscous and is described by

$$F = \eta\dot{\Delta}, \tag{1.4.2}$$

where dot indicates differentiation with respect to time. We refer reader to (Gross et al., 2006) for constitutive relation as well as other characteristics of the material. In our study, response of the material under cyclic loading is of particular interest as it reveals the rheological profile. The complex shear modulus is given by

$$\mu_m^c = \frac{F_0}{u_0}\frac{\imath s\mu}{\imath s + \frac{\mu}{\eta}}, \tag{1.4.3}$$

where $\imath$ is the imaginary unit. The Maxwell model is often used for description of viscoelastic deformation of icy bodies. The main advantage is its simplicity; viscosity of the dashpot is the actual effective (long-term) viscosity of the material and so can be experimentally measured. The model is well adapted for processes with forcing period close to Maxwell time $\tau_m = \frac{\eta}{\mu}$ but it fails when forcing covers wide range of frequencies.

1.4.2   Burgers material

If the period of loading differs from Maxwell time, other rheological models should be used instead of the Maxwell one. Based on laboratory experiments with frequencies larger than 10^{-4} Hz, Burgers rheology is one of the replacement candidates. It is proposed especially to describe transient deformations. The model is less commonly used and information about it is scattered in many sources. Therefore, in the following text we are going to summarize its main characteristics.

Burgers model can be represented by Maxwell model and Kelvin-Voigt model joined together in series as shown in Fig. 1.2. In addition to two parameters from Maxwell model, Burgers material is also characterized by a short-term viscosity η_k and a transient shear modulus μ_k. The secondary viscosity is suggested to follow the same rheological law as the primary one, i.e., the Arrhenius law, but with different reference viscosity. For the sake of simplicity, the shear moduli are often set equal. Using mechanical representation, the following equations for total stress and total deformation can be determined (subscripts
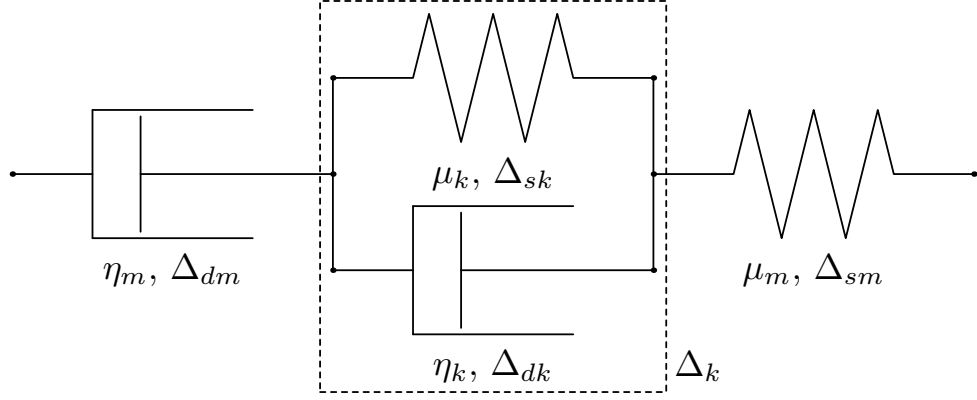
Figure 1.2: Mechanical representation of a Burgers model. Kelvin-Voigt element is shown in the dashed square.

s, d indicate spring and dashpot respectively)

$$\Delta = \Delta_{dm} + \Delta_k + \Delta_{sm}$$
$$\Delta_k = \Delta_{sk} = \Delta_{dk}$$
$$F = F_{dm} = F_k = F_{sm}$$
$$F_k = F_{sk} + F_{dk}.$$

Combining these equations we can derive the relation between stress, deformation and their time derivatives

$$
\begin{aligned}
F &= F_{sk} + F_{dk} \\
&= \eta_k \left(\dot{\Delta} - \dot{\Delta}_{sm} - \dot{\Delta}_{dm} \right) + \mu_k \left(\dot{\Delta} - \Delta_{sm} - \Delta_{dm} \right) \\
&= \eta_k \left(\dot{\Delta} - \frac{\dot{F}}{\mu_m} - \frac{F}{\eta_m} \right) + \mu_k \left(\Delta - \frac{F}{\mu_m} - \Delta_{dm} \right).
\end{aligned}
\tag{1.4.4}
$$

Differentiating eq. (1.4.4) with respect to time and rearranging the terms yields the desired constitutive relation

$$
\ddot{F}\eta_k\eta_m + \dot{F}\left(\mu_m\eta_m + \eta_k\mu_m + \mu_k\eta_m\right) + F\mu_m\mu_k = \ddot{\Delta}\mu_m\eta_m\eta_k + \dot{\Delta}\mu_m\mu_k\eta_m.
\tag{1.4.5}
$$

This is a second-order differential equation and so even without actually solving it for unit step deformation (stress-relaxation test) we can tell that the relaxation modulus will include two relaxation processes. That is one more than the Maxwell material. The extra dissipation peak due to additional process allowed Robuchon et al. (2010) to successfully despin Iapetus while explaining the flattening. These authors also considered Maxwell rheology but the model failed due to insufficient dissipation.

Rheological profile is a dynamic characteristic of material. The response of material to dynamic deformation is measured in oscillatory tests where the material is deformed

by simple harmonic waves. Using complex representation for the oscillations, deformation takes the form of

$$u(t) = u_0 \exp\left(\imath s t\right). \tag{1.4.6}$$

Under periodic deformation the response $F(t)$ is also periodic and can be written as

$$F(t) = F_0 \exp\left(\imath s t\right). \tag{1.4.7}$$

After substituting these forms into eq. (1.4.5), we obtain the complex shear modulus of Burgers model

$$\mu_b^c = \frac{F_0}{u_0} \imath s \mu_m \frac{\imath s + \tau_k}{\left(\imath s + \tau_m\right)\left(\imath s + \tau_k\right) + \imath s \frac{\mu_m}{\eta_k}}. \tag{1.4.8}$$

Here $\tau_k = \eta_k/\mu_k$ and $\tau_m = \eta_m/\mu_m$ are the two aforementioned relaxation times of Kelvin and Maxwell elements.

1.5 Iapetus

Iapetus is the third largest and the most distant regular satellite of Saturn. It has a mean density of $1083 \pm 13\,\mathrm{kg.m^{-3}}$ (Thomas et al., 2007). These authors consider a model with ice and rock densities of $930\,\mathrm{kg.m^{-3}}$ and $3000\,\mathrm{kg.m^{-3}}$. The value of mean density then translates into rock-to-ice fraction of 0.20. Iapetus has several interesting properties, some of which are unique in the Solar system.

Having discovered Iapetus in 1671, Giovanni Domenico Cassini noted that he could only see Iapetus clearly near western elongation but he could not detect it near eastern elongation. He concluded that one side of Iapetus' surface isn't capable of reflecting the Sun light. In 2007, inspection by the Voyager spacecraft revealed that the difference in reflectivity between the two hemispheres is of factor 5 to 6; the trailing bright side (Fig. 1.3(a)) has albedo 0.35, the leading dark side (also known as Cassini Regio) has albedo 0.07 (Morrison et al., 1975). This asymmetry of photometric properties between the hemispheres is the largest in the Solar system (Owen et al., 2001). The composition and the origin of the surfaces remain enigmatic even today. Neutral color of the bright side indicates presence of ices of water or ammonia, whereas red color of the dark side is suggestive of hydrate silicates, organic polymers, iron minerals, etc. In neither case the lack of spectroscopic data permits unique composition to be established. The theories about the origin of surface propose mostly formation by some external mechanism. Based on the calculations of the frequency of meteoric impacts, which peaked in the equatorial region of the leading side and was about half of the peak value in polar regions and on the trailing side, Cook and Franklin (1970) proposed that such selective destruction could have uncovered the dark rocky material hidden underneath the layer of ice. More recent theories explain the dark side by local deposition of the dust from Phoebe, Titan or even interplanetary dust.

Iapetus orbits on an almost circular orbit ($e = 0.0283$) in the distance of $3.51 \times 10^6\,\mathrm{km}$ from Saturn. It is in synchronous rotation with Saturn with the orbital/rotation period of $79.33\,\mathrm{days}$. Given such a large value of semi-major axis and D-dependence of the rate of

spin rate in eq. (1.2.6), the synchronicity is unexpected and it suggests stages with very dissipative interior in the evolution history of Iapetus.

The shape of Iapetus is best approximated by triaxial ellipsoid with equatorial radii a, b equal to 748.8 km, 743.2 km and polar radius c equal to 712.4 km (Thomas et al., 2007). Based on the mean density and the current spin rate, the flattening $a - c$ should be of only ~10 m. However, the observed flattening is 35.0 ± 3.7 km making it the largest non-hydrostatic anomaly known for the satellite larger than 1000 km in radius (Castillo-Rogez et al., 2007). The difference between the expected and actual flattening is well seen at 9 o'clock in Fig. 1.3(b).

Iapetus' shape corresponds to a body in the state of hydrostatic equilibrium with a rotation period of ~16 h in case of homogeneous interior or ~15 h in case of differentiated interior. Neither of these values agrees with the observed rotation period. To resolve this inconsistency, Castillo-Rogez et al. (2007) suggested that Iapetus preserved this shape as it despun into synchronous rotation by forming a lithosphere strong enough to resist the deformation from despinning. In the evolution scenario proposed by these authors, heat from SLRIs increased the temperature early in the history which led to a reduction of porosity and in turn to an increase of the conductivity of mantle. Consequently, strong lithosphere could have been formed. As the decay of SLRIs and LLRIs continued to warm the interior, tidal dissipation could start and despin the satellite into synchronous rotation.

It is noteworthy that these authors used purely conductive heat transfer, whereas Robuchon et al. (2010), who were also able to despin Iapetus and obtain the observed flattening, considered also convection. In both cases the success of calculation depended on the amount of radiogenic heating. Thus, the time of accretion of Iapetus could have been estimated. Castillo-Rogez et al. (2007) estimated the accretion time at $3.4 - 5.4$ Myr after the formations of CAIs. Robuchon et al. (2010) then placed the accretion at $2 - 4$ Myr after the formations of CAIs.

The last property that we mention is a high ridge in the equatorial region of Iapetus. This topographic feature, which is unique in the Solar system, was revealed by the Cassini mission (see Figs. 1.3(c), 1.3(d)). Visual observations established the length of ridge of at least 1600 km, width of ~20 km and height of ~18 km. In order to support such massive topography, the lithosphere has to be ~20 km thick. The ridge is heavily cratered which is suggestive of age similar to the surrounding terrain. Volcanic activity, tectonic activity and despinning were proposed as plausible explanations for the origin of the ridge. The connection between its formation and the shape of Iapetus has not yet been examined. However, in the investigations of flattening, existence of the ridge was always included by the constraint on minimal thickness of lithosphere.

In the remainder of this thesis we lay down the foundations for future exploration of the origin of the ridge by designing and testing a numerical method that can handle surface deformations due to thermal convection.

(a)   (b)

(c)   (d)
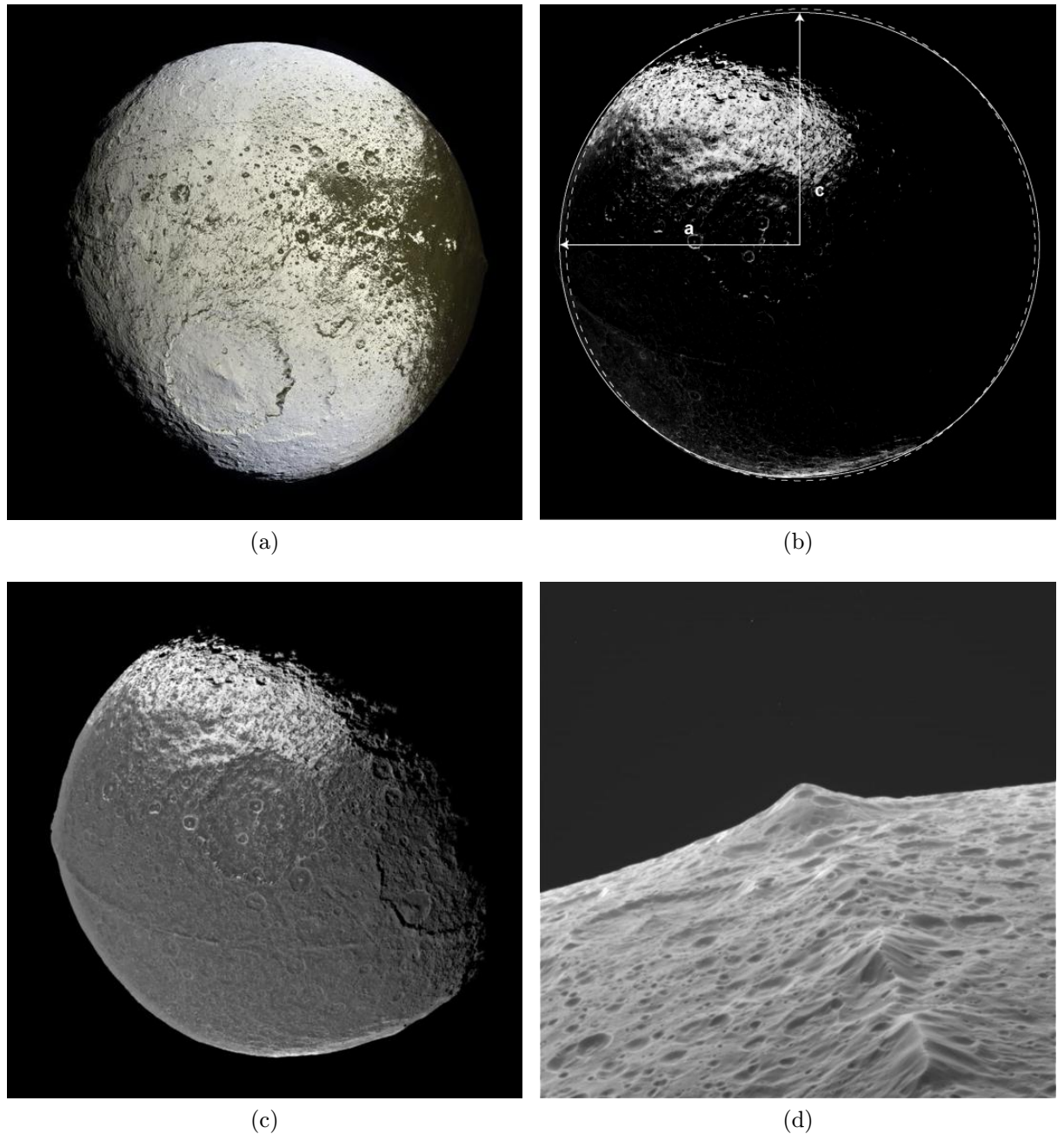
Figure 1.3: Notable features of Iapetus. (a) Bright trailing hemisphere and the transition to dark region captured by Cassini on September 10, 2007. (b) The dashed line indicates the hypothetical shape of the body in hydrostatic equilibrium with rotation period of 79.33 days, the solid line indicates the actual surface. Captured by Cassini on December 31, 2004. (c) The length of the ridge in picture (by Cassini from December 31, 2004) can be traced to 1300 km. The ridge runs parallel to the equator within couple of degrees. On the western horizon, the peak of the ridge has an elevation of at least 13 km. (d) Close flyby a few thousand kilometers above the surface by Cassini on September 10, 2007 showing the detail of the ridge. Highest peaks are 10 km above the surrounding terrain. Picture credits: (b) (Castillo-Rogez et al., 2007); (a), (c), (d) NASA/JPL/Space Science Institute.

Chapter 2

Model

A realistic mathematical model of Iapetus capable of accurate description of the ridge formation is very complex, as it has to include the nonlinear rheology, the despinning and the radiogenic heating. In addition, the model has to be formulated on the time-dependent domain. In this work, our objective is not as bold as explaining the origin of the mysterious ridge. We are focused on designing the numerical method that can simulate thermal convection and the deforming surface. For this purpose we use a model of Iapetus that is of less complexity, yet includes all the characteristic necessary for thorough testing of our numerical method. In this chapter we derive the simplified model from general balance laws.

2.1 Balance laws

We will begin by summarizing the equations of conservation of the mass, the linear momentum, the energy and the angular momentum using material description (e.g., Ricard (2007), the used symbols are listed in Table 2.1):

$$\frac{\mathrm{D}\rho}{\mathrm{D}t} + \rho\nabla\cdot\vec{v} = 0, \tag{2.1.1}$$

$$\rho\frac{\mathrm{D}\vec{v}}{\mathrm{D}t} = \nabla\cdot\boldsymbol{T} + \rho\vec{f}, \tag{2.1.2}$$

$$\rho C_v\frac{\mathrm{D}T}{\mathrm{D}t} = -\nabla\cdot\vec{q} + \boldsymbol{T}:\nabla\vec{v} + \rho H \tag{2.1.3}$$

$$\boldsymbol{T} = \boldsymbol{T}^T. \tag{2.1.4}$$

To complete the system of eqs. (2.1.1)-(2.1.4), rheological properties and equation of state of the material must be provided. Based on physical considerations about the problem and our interest to reduce the complexity of the realistic model, we make the following simplifications to the system:

1. We consider water ice to be incompressible.

2. We assume that time and spatial variations of velocities as well as velocities themselves are small, so that inertia can be neglected. This is a common argument in

geophysics because on Earth, these quantities can be measured and proven to be negligible. There are no such results for Iapetus but we use the assumption in our model anyway and in Chapter 5 provide an *a posteriori* justification. *A priori* justification can be made using the dimensionless form of the momentum equation (e.g., Ricard (2007)); the term becomes negligible if Ra $\ll$ Pra. Here Ra is the thermal Rayleigh number

$$\text{Ra} = \frac{d^3 \Delta T \rho_0 \alpha_0 g_0}{\eta_0 \kappa_0}$$

and Pra is the Prandtl number

$$\text{Pra} = \frac{\eta_0}{\rho_0 \kappa_0}.$$

The subscript 0 indicates the reference value. In our case $\text{Ra}/\text{Pra} = 1/10^7$.

3. The vector of body forces consists of gravitational force and centrifugal force only. We neglect Coriolis force and Poincaré acceleration because even for Iapetus rotating with the spin rate close to Roche limit (3.8 h, Castillo-Rogez et al. (2007)), these effects are orders of magnitude smaller in comparison to gravity and centrifugal force. For our scaling argument, we use the surface gravity of Iapetus $g = 0.2\,\text{m.s}^{-2}$, its outer radius $a = 750\,\text{km}$, angular velocity corresponding to Roche limit and characteristic velocity $U = 1\,\text{m.yr}^{-1}$, which is hundred times larger than on Earth. Consequently, we obtain the comparison of magnitudes of the forces

$$\frac{\text{centrifugal}}{\text{Coriolis}} = \frac{\omega^2 a}{2\omega U} = \frac{1}{10^{-9}},$$
$$\frac{\text{gravity}}{\text{centrifugal}} = \frac{g}{\omega^2 a} = \frac{1}{200}.$$

Moreover, we neglect self-gravitation. Finally, we make our first complexity-reducing simplification; we consider centrifugal force that is constant in time instead of the evolving centrifugal force given in eq. (1.2.6).

4. The second complexity-reducing simplification is the assumption that the deformations in mantle can be approximated as deformations of incompressible, Newtonian fluid with temperature-dependent viscosity and so rheological description in eq. (1.3.4) can be used. Furthermore, we utilize the simplified form of the Arrhenius law

$$\eta = \eta_0 \exp\left(-a_{\text{vis}} T\right),$$

where a_{vis} is a positive dimensionless constant.

5. We consider density to be only a linear function of temperature. The equation of state then takes the form

$$\rho = \rho_0 \left(1 - \alpha \left(T - T_0\right)\right).$$

This assumption does not contradict Assumption 1., where we consider fluid to be mechanically/isothermally incompressible. Here, we consider it to be thermally compressible. Due to small thermal expansion of water ice, the variations of density are less than 1%. The reference temperature T_0 is uniform ans so following Ricard (2007) we can choose $C_v = C_p$.

6. In the balance of energy we assume Fourier's law $\vec{q} = k\nabla T$. Furthermore, due to Assumption 4., the term $\boldsymbol{T} : \nabla\vec{v}$ reduces only to $\boldsymbol{\sigma} : \nabla\vec{v}$. This term is known as viscous dissipation. Following Robuchon et al. (2010) we do not include it in our model as according to their calculations, the term is negligible compared to the radiogenic power which is the dominant source of heat. In our model the radiogenic heat rate does not follow eq. (1.2.4). Instead, as our third and final complexity-reducing simplification, we chose to warm the mantle from below.

2.2 Governing equations

Imposing all the simplifications on the balance laws, the equation of state and the rheological relation yields the governing equations of our model (see Table 2.1 for meaning of symbols)

$$
\left.
\begin{aligned}
\nabla \cdot \vec{v} &= 0 \\
-\nabla\pi + \nabla \cdot \left(\eta \left(\nabla\vec{v} + (\nabla\vec{v})^{\mathrm{T}} \right) \right) + \rho\vec{f} &= 0 \\
\rho_0 C_p \left(\frac{\partial T}{\partial t} + \vec{v} \cdot \nabla T \right) &= \nabla \cdot (k\nabla T)
\end{aligned}
\right\} \quad \Omega_t \times (0, T], \qquad (\star)
$$

where

$$
\begin{aligned}
\rho &= \rho_0(1 - \alpha(T - T_0)), \ \alpha = const > 0, \\
\eta &= \eta_0 \exp(-a_{\mathrm{vis}}T), \ a_{\mathrm{vis}} = const > 0, \\
k &= const > 0, \ C_p = const > 0, \\
\vec{f} &= \vec{g}(|\vec{x}|) + \vec{b}(\vec{x}).
\end{aligned}
$$

If we kept inertia in balance of linear momentum, the governing equations would constitute the Oberbeck-Boussinesq approximation (e.g., Feireisl and Novotný (2009)). The continuity equation and the momentum equation in system $(\star)$ are known as the Stokes problem. Because of the use of Fourier's law in the conservation of energy, that equation in system $(\star)$ is known as the Fourier problem.

For the space variables, we do not consider the full 3D problem, but instead restrict ourselves to time dependent domain Ω_t that lies in a half-plane defined by the axis of rotation of Iapetus and a random point in its mantle (Fig. 2.1). This axisymmetric approximation is meaningful, as both the ridge and the volume forces have rotational symmetry. Thus, we obtain a 2D problem for which the choice of polar coordinates is natural. The domain of our model is then the cylinder with base Ω_t.
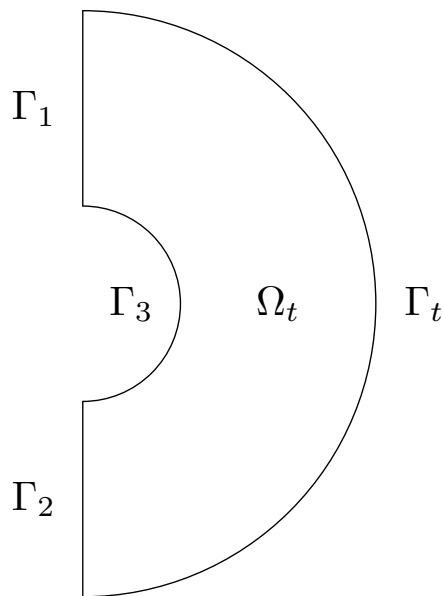
Figure 2.1: Time-dependent base of the model domain.

2.3 Boundary and initial conditions

In order to solve the system ($\star$) we must provide boundary and initial conditions. Boundaries Γ_1 and Γ_2 are virtual. The conditions that we prescribe on them express our requirement of axial symmetry of the velocity and temperature fields.

$$v_\theta = 0 \qquad \frac{\partial v_r}{\partial \theta} = 0 \qquad \frac{\partial T}{\partial \theta} = 0 \qquad \text{on} \qquad (\Gamma_1 \cup \Gamma_2) \times [0, T] \qquad (2.3.1)$$

Boundary Γ_3 is physical. We prescribe the boundary as impermeable and heated with constant temperature T_{core}. We would like to remind the respected reader that while the no-slip condition is perfectly valid, the prescribed temperature is a simplification that replaces the radiogenic heating.

$$\vec{v} = \vec{0} \qquad T = T_{\text{core}} \qquad \text{on} \quad \Gamma_3 \times [0, T] \qquad (2.3.2)$$

Boundary Γ_t is the deformed boundary where the ridge is formed. Here we prescribe a constant temperature T_{space} and zero surface force, which is defined as a projection of the stress tensor into the direction of outward normal to the surface. This means that there are no surface forces acting on the boundary which can then deform freely.

$$\boldsymbol{T} \cdot \vec{n} = \vec{0} \qquad T = T_{\text{space}} \qquad \text{on} \quad \Gamma_t \times [0, T] \qquad (2.3.3)$$

As this model's ambition isn't to accurately describe the ridge formation, the initial conditions are not based on realistic accretional temperature profile in eq. (1.2.1). Instead, for the purpose of testing our numerical method, we use different (even discontinuous) initial conditions. These temperature profiles are specified in Chapter 4.

Symbol	Meaning
$\vec{v}$	vector of velocity
ρ	density
π	pressure
$\boldsymbol{T}$	Cauchy stress tensor
$\boldsymbol{\sigma}$	deviatoric part of Cauchy stress tensor
$\dot{\boldsymbol{\epsilon}}$	strain rate tensor
t	time
T	temperature
η	viscosity
$\vec{f}$, $\vec{g}$, $\vec{b}$	volume, gravitational and centrifugal force
H	heat production per unit volume
$\vec{q}$	heat flux
k	conductivity
C_p, C_v	specific heat capacity at constant pressure/volume
$\kappa = \frac{k}{\rho C_p}$	thermal diffusivity
α	thermal expansion coefficient
ω	spin rate
$\vec{n}$	outer-pointing normal to the boundary
d	characteristic length

Table 2.1: Table of symbols.

The simplified model describes the flow of linear, highly viscous fluid with temperature-dependent viscosity that is driven by centrifugal force and thermal buoyancy. The flow is modeled inside the deforming spherical shell. Temperature-dependent viscosity and external heating allow the model to describe vigorous convection that was likely to occur inside Iapetian mantle. Due to free outer boundary, the model can capture large scale deformations caused by the centrifugal force. Thus, with exception of the effects due to nonlinear rheology, the simplified model can describe all the important phenomena related to the formation of the ridge. This fact make it a well-suited candidate for testing our numerical method. We argue that as long as the method performs reasonably well in conditions of the simplified model, it is also very likely to succeed when applied to realistic model of Iapetus. In the rest of the thesis we therefore examine the simplified model.

Chapter 3

Surface Tracking

This chapter describes two different approaches that we used for description of the moving boundary. After a brief overview of existing methods, we explain the method due to Gerya that inspired our first approach. After its description, a discussion follows of the reasons why it failed. We then introduce our second and successful approach. The last section outlines the problems with existence and regularity of classical and weak solutions that are due to free surface.

3.1 Overview of methods

The crudest classification divides surface tracking methods into those working with Lagrangian grids and those that use Eulerian grids. Lagrangian grid methods construct a grid that moves with the fluid, thus automatically traces the surface. These methods are mostly utilized by finite-element methods (FEM). Their main disadvantage is the computational cost of regridding techniques that have to be employed when the deformations are too big. Eulerian grid methods work on a fixed Eulerian grid and are therefore more suitable for finite-difference methods (FDM). We review this class in greater detail, as our numerical method is based on the FDM.

Two of the most applied Eulerian grid methods are marker-and-cell method (MAC) and volume-of-fluid of method (VOF). There are two features that these methods have in common. First, the computational domain is extended to contain the model domain by adding some artificial nodes and this new domain is fixed. Second, the methods track surface indirectly by following the changes in volume of the fluid. For this purpose the term *cell* is defined as a group of Eulerian nodes.

Volume-of-fluid method

In every cell, the volume-of-fluid method (Hirt and Nichols, 1981) defines a scalar quantity ϕ, *volume fraction*, that takes values between zero and one depending on the type (location) of the cell. In the full cell that lies inside the fluid we set $\phi = 1$, while in the empty cell located outside the fluid we set $\phi = 0$. The cells with $\phi \in (0, 1)$ and at least one empty neighboring cell are treated as interface cells and are used to locate the surface.

The surface evolves according to the basic kinematic equation

$$\frac{\partial \phi}{\partial t} + \vec{v} \cdot \nabla \phi = 0. \tag{3.1.1}$$

Due to hyperbolic nature of this equation, numerical solution can be seriously affected by numerical effects if the appropriate scheme is not used. Oscillations could produce meaningless values of volume fraction ($\phi > 1$), while diffusion could smear the sharp gradients needed for accuracy of the method.

Even with accurate scheme, the resolution of VOF method is lower compared to other methods. This is due to surface location being stored only in the cells. Better resolution could be achieved on a finer grid but at higher computational expenses. Another weak spot of the method is the nontrivial calculation of surface curvature and normals which are important for prescription of boundary conditions at the moving boundary.

Markers-at-cell method

Markers-at-cell method (e.g., McKee et al. (2008)) improves on the resolution of VOF method by tracing the surface with Lagrangian particles/markers. The markers are advected by the velocity field according to

$$\frac{\mathrm{d}\vec{x}^i}{\mathrm{d}t}(t) = \vec{v}(\vec{x}^i, t), \tag{3.1.2}$$

where $\vec{x}^i(t)$ is the position of i-th marker at time t and $\vec{v}(\vec{x}^i, t)$ is its velocity. The location of surface is reconstructed by different techniques using markers' positions (e.g., weighted interpolation). Cells are classified according to the concentration of fluid markers or void markers they contain. The cell is pronounced full if it contains fluid markers exclusively and empty if it is filled with void markers. Cells containing mixture of markers are the interface cells. The classification serves the purpose of identifying the cells where boundary conditions must be prescribed. Even with the additional information about the location of surface between the interface cells, calculation of normals is not a straightforward operation.

Apart from increased CPU requirements connected with the accommodation of markers, the main weakness of MAC method is the fact that markers can be pulled apart by certain kind of flows. Thus, voids can be created that give misleading picture of the surface.

Variable-density approximation

For neither of the methods normal calculation is a trivial task. Once the normal to surface is known, the questions arises how much of an error is made when the condition in eq. (2.3.3) is discretized into the grid nodes. To avoid difficulties due to normals, simplified boundary conditions could be prescribed on the moving boundary (e.g., assume that the surface remains spherical by $\vec{n} = \vec{e}_r$). This simplification, however, does not treat the essential problem of Eulerian grid methods; the dynamically changing system matrix.

The number of Eulerian nodes, i.e., the number of unknowns, is constant because of the fixed size of the computational domain. Meanwhile, the type of equations changes as the deformed fluid contains different full and surface cells. Thus, structure of matrix of the system evolves. Depending on the boundary conditions, adjusting the matrix can be quite costly. Therefore, some methods make use of the variable-density approximation.

This approach originated in studies of flow near the interface of two fluids with high density contrast. The main idea is to solve the governing equations of the thicker fluid in a whole region occupied by the two fluids. In this way we treat the problem as a flow of a single fluid with variable density and so there is no need for boundary conditions on the interface. In practice, there are two reasons why this approach can fail. First one is down to the fact that for iterative solvers, high density contrast affects the rate of convergence and so the solution might not even converge. The second reason is connected with different character of flows in the interface region. It is possible that there might even be a discontinuity of tangential velocities at the interface. Thus, if an averaging method for calculating the velocities for advection is chosen poorly, unrealistic movements of surface could be introduced.

3.2   Method of Gerya

Large scale problems in geophysics (e.g., collisions of tectonic plates) are modeled as flow of multiple fluids with high density and viscosity contrast. Since such diverse properties give rise to instabilities, the numerical method applied must be robust. Also, the often peculiar shapes of regions occupied by different fluids require a method with great resolution. One of the most successful methods used is the method by Gerya (Gerya and Yuen, 2003).

The approach is based on MAC method with some aspects of the variable-density approximation. The method defines as many types of markers as there are types of fluid within the computation domain. Markers have the material properties of the fluid they represent. In addition to tracking the interfaces, markers are also used to solve the Fourier problem in system ($\star$). With their help the difficulties caused by the advection term $\vec{v} \cdot \nabla T$ are overcome (the reader is referred to (Gerya, 2010) for more details).

Key feature of the approach is the interpolation between markers and Eulerian nodes. The velocities used to advect markers are computed in nodes and then interpolated by distance-weighted averaging to markers. For each marker, a zone is defined, that contains the nodes used for interpolation. Material properties prescribed in material nodes are given by distance-weighted averaging of material properties of markers included in the interpolation region of the node (see Figs. 3.1(a) and 3.1(b) for illustration of the process on the staggered grid). Because of the interpolation, governing equations that use the values defined in nodes, do not *feel* the discontinuity of material properties that would otherwise be located on the interface. We believe that part of the success of the method can be attributed to this procedure. The other part is probably associated with adjusting the velocity interpolation in such a way, that the values possibly producing unrealistic movements of interface are omitted.

According to Gerya (2010), the method can also be used to model deformations of
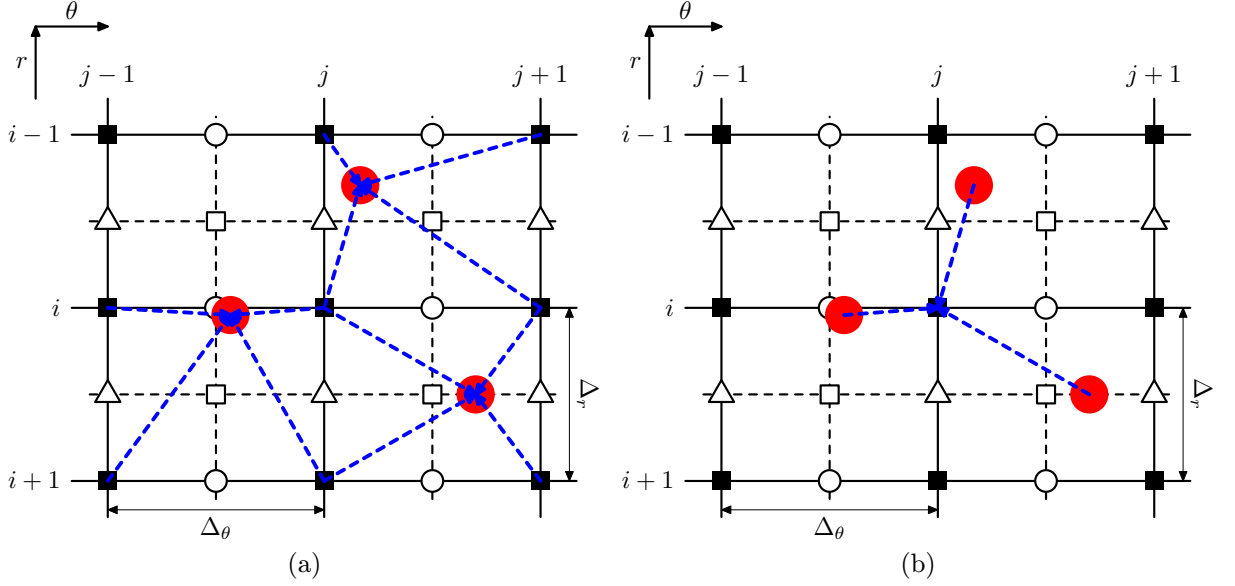
Figure 3.1: Interpolation between markers and Eulerian nodes. (a) Velocities are interpolated from node to markers. In this case, the velocity is defined in a full black square node and interpolation region of the marker is bounded by four nearest velocity nodes. (b) Material properties are interpolated from markers to node. In this case, material properties are defined in a full black square node and the interpolation region of the node is bounded by the nearest nodes of the same kind.

the surface. To replicate the method's original setting, the body is surrounded by a weak medium that has much smaller density ($\rho \ll 1\,\mathrm{kg.m^{-3}}$) and much smaller viscosity than the deformed object.

3.3 Surface markers method

Our first approach to solving the system ($\star$) was based on the method of Gerya which is modified for modeling surface deformations following the last section. We make several alternations to the proposed method:

1. We use a single type of tracers; the *surface markers*. As we show in Chapter 4, our numerical method for the heat equation is robust. Thus, we do not need markers to resolve the issues due to advection term. The surface markers are used solely to locate the surface.

2. We perform spline interpolation to define surface between the markers. The interface should therefore be sharper compared to the original method where it is located by interpolating the positions of numerous kinds of markers.

3. We only interpolate velocities from the nodes to the markers. No nodes are omitted from the interpolation. The surface markers are advected according to eq. (3.1.2).
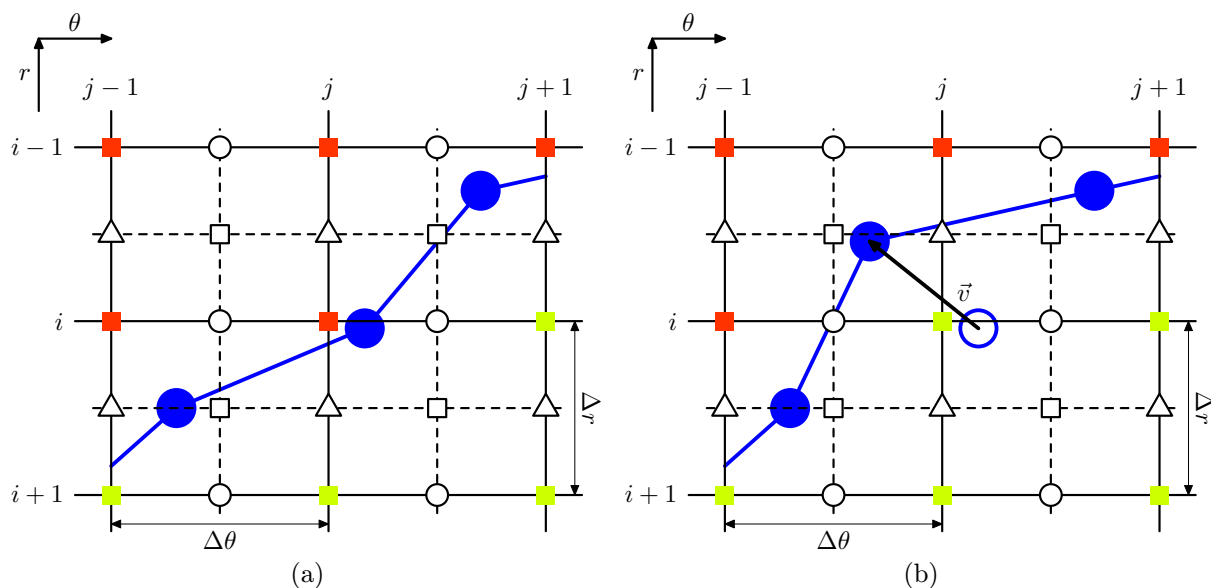
Figure 3.2: Definition of material properties. (a) Node (i, j) carries properties of the weak medium as it is located above the surface represented by the blue line. (b) Marker is advected with velocity $\vec{v}$. Node (i, j) is now below new surface and receives the material properties of mantle.

4. In addition to small viscosity and density the weak medium has high conductivity, so that thermal boundary condition prescribed on the fixed boundary of extended domain can be conducted to the interface.

5. Material properties are set in Eulerian nodes. A material node located below the interface obtains the properties of mantle, whereas a node above the interface gets properties of the weak medium (Fig. 3.2). Thus, there is no smoothing of the parameters near the interface.

The above presented version of the method, however, fails to model the deforming surface. As shown in Fig. 3.3, the shape of surface is faulted with unrealistic oscillations. The oscillations appear when mantle/weak medium material nodes are about to change character with the translation of interface. The discontinuity of material parameters that the system suddenly *feels* is responsible for the oscillations. Since the method includes no filter or damping, these oscillations propagate and eventually ruin the whole solution.

As the description suggests there are at least two solutions to this problem. First, a larger radial spatial step could be used. If possible, the distance between the material nodes should be chosen in such a way that a strip these nodes define would accommodate the surface at all times. Thus, no node would change character. This approach could be meaningful for methods that can handle variable spatial step size. Otherwise it implies sparser grid which results in less accurate solution of Stokes-Fourier system. The second approach is to smooth the material parameters near the interface of the body and the weak medium.
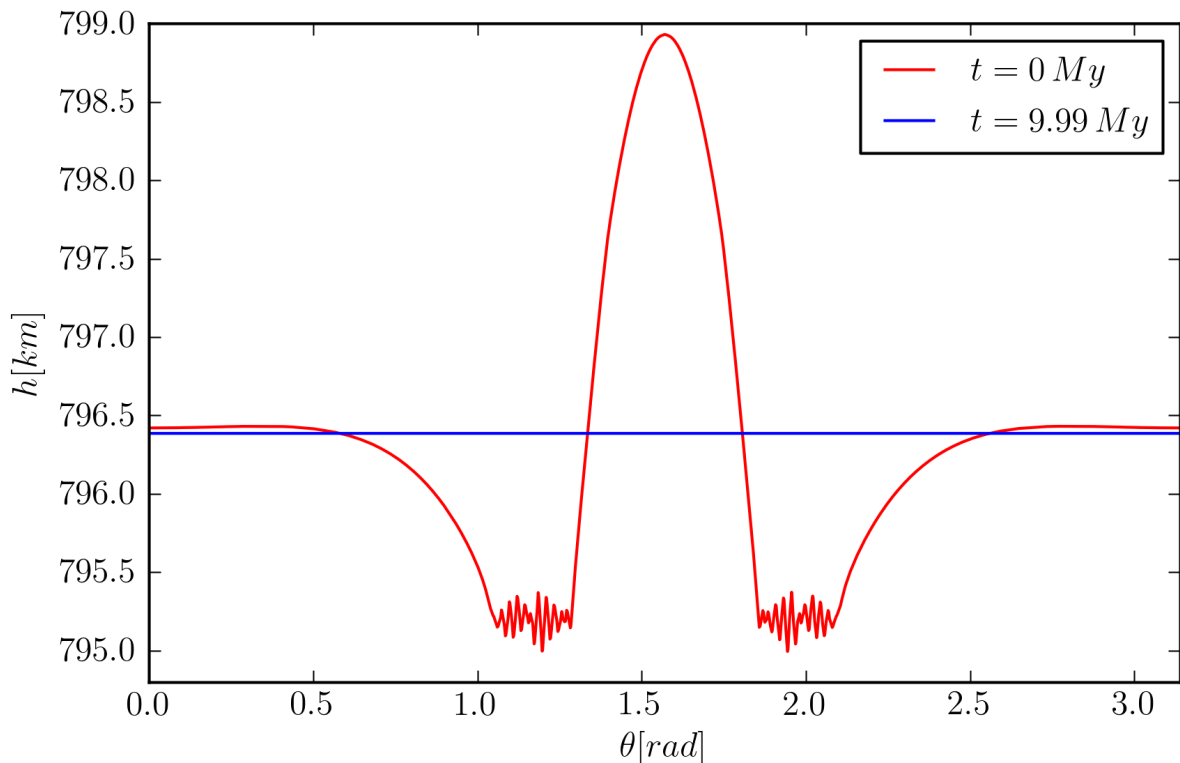
24

Figure 3.3: Oscillations in the interface. Rising equatorial plume creates a central ridge while falling side currents create valleys near $\theta = 1.2$ and $\theta = 2.0$. The oscillations arise as mantle material nodes are about to be included in the weak medium region. The simulation parameters: time step $\Delta t = 10^3$ yr, Rayleigh number Ra $= 10^5$ and radial spatial step $\Delta r \sim 4.8$ km.

We do not implement the treatment to oscillations into surface markers method. Neither do we implement here the modification that would prevent creation of voids due to markers being driven apart by divergent flows, which we observed in some numerical experiments. Instead, we design a new approach with the listed weak spots in mind.

3.4   Surface height method

Our second approach to problem ($\star$) belongs to the class of surface tracking methods (e.g., Hyman (1984)). Unlike MAC methods or VOF methods, these methods trace the deforming surface directly. In this section we explain how our method locates and evolves the surface and how it handles the boundary conditions.

The surface is defined as an implicit material surface $H(r, \theta, t) = 0$. The observations of current shape of Iapetus do not suggest dramatic deformations in the history. Therefore, we assume that at every time t conditions of the implicit function theorem (e.g., the surface is not multivalued with respect to θ) hold and we can express the height of surface

explicitly as

$$r = h(\theta, t). \tag{3.4.1}$$

Obviously, this method of tracing is not affected by diverging flows. The surface evolves according to

$$\frac{\partial H}{\partial t} + \vec{v} \cdot \nabla H = 0, \tag{3.4.2}$$

which is a necessary and sufficient condition for material surface to stay material (see (Maršík, 1999) for proof).

The difficulties due to moving boundary are overcome by applying the variable-density approximation. The computational domain Ω pictured in Fig. 3.4(a) is extended in such a way that $\forall t \in [0, T] : \Omega \supset \Omega_t$. We only replace part of the boundary Γ_t so that $\partial \Omega = \Gamma_1 \cup \Gamma_2 \cup \Gamma_3 \cup \Gamma_4$. The new domain is fixed. On solid boundary Γ_4 we prescribe no-slip boundary condition and a fixed temperature.

$$\vec{v} = \vec{0} \qquad T = T_{\text{space}} \qquad \text{on} \quad \Gamma_4 \times [0, T] \tag{3.4.3}$$

For a fixed time t we divide the computational domain into two disjoint regions using the known position of surface (interface)

$$\text{ice} := \{\vec{x} = (r, \theta) \in \Omega \mid r < h(\theta, t)\},$$
$$\text{air} := \{\vec{x} = (r, \theta) \in \Omega \mid r \geq h(\theta, t)\}.$$

Material parameters in these regions differ and the discontinuity is located on the surface

$$\rho(\vec{x}, T) = \begin{cases} \rho_{0,\text{ice}}(1 - \alpha(T - T_0)) & \vec{x} \in \text{ice} \\ \rho_{0,\text{air}} & \vec{x} \in \text{air} \end{cases}$$

$$\eta(\vec{x}, T) = \begin{cases} \eta_{0,\text{ice}} \exp(-a_{\text{vis}} T) & \vec{x} \in \text{ice} \\ \eta_{0,\text{air}} & \vec{x} \in \text{air} \end{cases}$$

$$\alpha = const > 0,$$
$$a_{\text{vis}} = const > 0.$$

We set $\rho_{0,\text{air}} \ll \rho_{0,\text{ice}}$, $\eta_{0,\text{air}} \ll \eta_{0,\text{ice}}$ to obtain high contrast required by variable-density approximation. To avoid oscillations, we smooth the density discontinuity. We use linear extrapolation and restrict the smoothing only to air nodes in immediate neighborhood of the interface. The process is illustrated in Fig. 3.4(b). Since in our numerical experiments, the discontinuous viscosity does not seem to cause difficulties, we keep this interface sharp.

The essence of using variable density and viscosity is to approximate the Stokes problem in ($\star$). For this problem, the boundary conditions on free surface are quite complex. In addition, the problem is solved using three types of nodes of the staggered grid. On the other hand, the heat equation uses only single type of nodes and the boundary condition that we chose is simple enough so that we can prescribe it with reasonable accuracy at the interface Γ_t. Thus, there is no need to use variable conductivity as in our first approach. Surface temperature T_{space} is in fact prescribed in the whole air region. The choice is
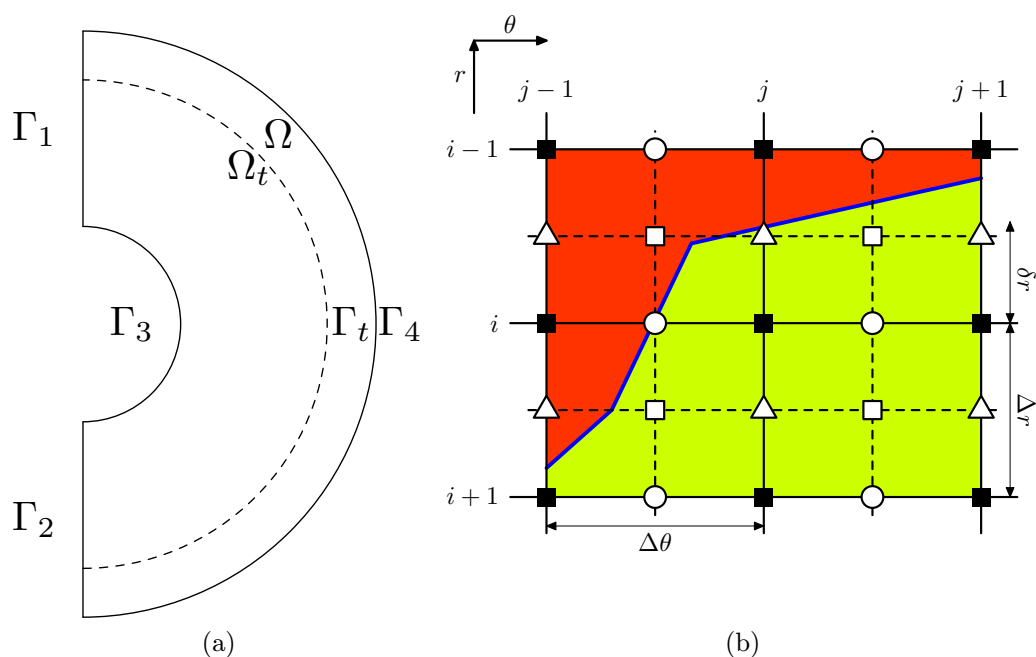
Figure 3.4: Surface height method. (a) The computational domain Ω is fixed and contains the model domain Ω_t. (b) Discontinuity of density at the interface is smoothed by linear extrapolation. The value in node $(i-1, j)$ is set according to $\rho(r_{i-1}, \theta_j) = \frac{\delta r}{\Delta r}\rho(r_i, \theta_j)$.

meaningful as this region represents the universe that surrounds Iapetus which is likely to have constant temperature because of its huge distance from the Sun.

We treat the two weaknesses of variable-density approximation mentioned in Section 3.1 in the following way. Instead of an iterative solver, we use a direct one (type of Gauss elimination implemented in UMFPACK). Instead of interpolation, the material velocities for eq. (3.4.2) are obtained by extrapolating the velocities from ice nodes. We use simple polynomial extrapolation from two nodes. Results of numerical experiments with this method are presented in Chapter 5.

3.5 Remarks on existence and regularity

Modern theory of partial differential equations focuses on the existence and regularity of weak solutions rather than classical solutions. The obtained results are very useful for the FEM methods, as their very essence is the weak (integral) formulation. Classical-formulation-based FDM methods are used in geophysical modeling with great success but, unlike the FEM methods, they often lack the rigorous mathematical justification. In this sections we outline the difficulties we face when trying to provide the support for usage of FDM for our problem ($\star$).

The justification attempt consists of two steps. First, we seek a regularity result for the system ($\star$) as we want make use of the embedding Theorem 3.5.1:

Theorem 3.5.1. *Assume that $\Omega \in \mathbb{R}^n$ is a bounded domain with sufficiently smooth boundary, $1 < p < \infty$, $m \in \mathbb{Z}_+$ and*

$$k < m - \frac{n}{p}.$$

Then

$$W^{m,p}(\Omega) \hookrightarrow\hookrightarrow C^k(\Omega).$$

In order to apply the theorem we would consider fixed bounded domain $\Omega \supseteq \Omega_t, \forall t \in [0, T]$ and extend the solution smoothly.

Classical solution of system ($\star$) requires $\vec{v}(\bullet, t) \in C^2(\overline{\Omega})^2$. Since in our case $n = 2$, $p = 2$ we want $m > 3$. Unfortunately, there is no such regularity result available for our system. In fact there are no results that establish existence let alone regularity even for much simpler systems that are formulated on the evolving domain.

To avoid the issue with moving boundary, we might try to research regularity of solution to the approximate problem formulated in Section 3.4. However, material properties in regularity estimates for similar systems with fixed domain must not be discontinuous (e.g., Bulíček et al. (2011) require at least continuous viscosity for evolutionary Stokes-Fourier system). We could regularize material properties by suitable mollifiers, but still, we would not be able to establish the regularity result $\vec{v}(\bullet, t) \in W^{3,2}(\Omega)^2$. The result is essentially a requirement for velocity field to be contained in some Bochner space. In order to prove it, the term $\frac{\partial \vec{v}}{\partial t}$ would have to be included into the momentum equation and the term $\boldsymbol{\sigma} : \nabla \vec{v}$ would have to be included into the heat equation so that appropriate energy estimates could be made. Since, our argument for neglecting these terms from the original balance laws is based on scaling, adding them back should not affect the solution.

In the second step, we would seek an equivalent of Serrin's result *'certain weak solutions of the time dependent Navier-Stokes equations must actually be solutions in an ordinary sense'* (Serrin, 1962) for our system.

The existence of results described above would mean that there exists a strong sufficiently regular solution and application of FDM would thus be mathematically justified.

Chapter 4

Numerical Methods

In this chapter we describe a method for obtaining the numerical solution to approximation of the Stokes-Fourier system described in Section 2.2. Separate sections are devoted to methods for Stokes problem, the heat equation and the advection of surface. We also analyze the stability of numerical schemes used to solve the evolutionary equations of the system.

4.1 Introduction

Application of variable-density approximation to system ($\star$) leads to an approximate problem that we outlined in Section 3.4. It is this new problem that we solve with our numerical method. For the sake of clarity we begin the discussion of method by definition of the approximate problem.

4.1.1 Approximate problem

Governing equations

In a fixed domain $\Omega \times (0, T]$, $\Omega \in \mathbb{R}^2$, $\partial\Omega = \Gamma_1 \cup \Gamma_2 \cup \Gamma_3 \cup \Gamma_4$ (Fig. 3.4(a)) we solve the stationary Stokes-Fourier system

$$\nabla \cdot \vec{v} = 0, \tag{4.1.1}$$

$$-\nabla\pi + \nabla \cdot \left(\eta\left(\nabla\vec{v} + (\nabla\vec{v})^{\mathrm{T}}\right)\right) + \rho\vec{f} = 0, \tag{4.1.2}$$

$$\rho_{0,\mathrm{ice}}C_p\left(\frac{\partial T}{\partial t} + \vec{v}\cdot\nabla T\right) = \nabla \cdot (k\nabla T), \tag{4.1.3}$$

where

$$\rho(\vec{x}, T) = \begin{cases} \rho_{0,\text{ice}}(1 - \alpha(T - T_0)) & \vec{x} \in \text{ice} \\ \rho_{0,\text{air}} & \vec{x} \in \text{air} \end{cases} \quad (4.1.4)$$

$$\eta(\vec{x}, T) = \begin{cases} \eta_{0,\text{ice}} \exp(-a_{\text{vis}}T) & \vec{x} \in \text{ice} \\ \eta_{0,\text{air}} & \vec{x} \in \text{air} \end{cases} \quad (4.1.5)$$

$$\vec{f} = \vec{g}(|\vec{x}|) + \vec{b}(\vec{x}) \quad (4.1.6)$$

with α, a_{vis}, k, C_p, $\rho_{0,\text{air}}$, $\rho_{0,\text{ice}}$, $\eta_{0,\text{air}}$, $\eta_{0,\text{ice}}$ all constant and $\rho_{0,\text{air}} \ll \rho_{0,\text{ice}}$, $\eta_{0,\text{air}} \ll \eta_{0,\text{ice}}$.

The ice and air regions are determined by the location of surface at a fixed time t. If the position of surface is expressed explicitly in polar coordinates ($\vec{x} = (r, \theta)$) as

$$r = h(\theta, t) \quad (4.1.7)$$

the ice and air regions are defined as

$$\text{ice} := \{\vec{x} \in \Omega \mid r < h(\theta, t)\},$$
$$\text{air} := \{\vec{x} \in \Omega \mid r \geq h(\theta, t)\}.$$

The surface evolution is an initial value problem

$$\frac{\partial h}{\partial t} + \frac{v_\theta}{r} \frac{\partial h}{\partial \theta} = v_r, \quad (4.1.8)$$
$$h(\theta, 0) = h_0(\theta)$$

that we solve in domain $[0, \pi] \times (0, T]$. Here $h_0(\theta)$ is the initial position of surface and v_r, v_θ are radial and tangential components of velocity.

Boundary and initial conditions

Boundary conditions of the approximate problem and exact problem ($\star$) remain unchanged for segments Γ_1, Γ_2, Γ_3.

$$v_\theta = 0 \qquad \frac{\partial v_r}{\partial \theta} = 0 \qquad \frac{\partial T}{\partial \theta} = 0 \qquad \text{on} \qquad (\Gamma_1 \cup \Gamma_2) \times [0, T] \quad (4.1.9)$$
$$\vec{v} = \vec{0} \qquad T = T_{\text{core}} \qquad \text{on} \quad \Gamma_3 \times [0, T] \quad (4.1.10)$$

In the new domain, the moving boundary Γ_t with prescribed free surface boundary condition is replaced by a fixed boundary Γ_4 which is impermeable and cooled to a constant temperature T_{space}.

$$\vec{v} = \vec{0} \qquad T = T_{\text{space}} \qquad \text{on} \quad \Gamma_4 \times [0, T] \quad (4.1.11)$$

We use three types of initial conditions. The first temperature profile is continuous and is given as symmetrically perturbed conductive profile

$$T_0(r, \theta) = A + \frac{B}{r} + \frac{\Delta T}{100} \left(\frac{3}{2} \cos^2(\theta) - \frac{1}{2} \right) \sin\left(-\frac{\pi}{\log(R_n)} \log\left(d \frac{1 - R_n}{r R_n} \right) \right), \quad (4.1.12)$$

where $\Delta T = T_{\text{core}} - T_{\text{space}}$. Fraction $R_n = R_1/R_2$ is the ratio of inner and outer radii of Ω, d is then the characteristic length. Constants A and B are set such, that the conductive profile $A + B/r$ is equal to T_{core} for $r = R_1$ and T_{space} for $r = R_2$. Clearly, this is a continuous initial condition. The remaining initial conditions are based on discontinuous profile

$$T(r) = \begin{cases} T_{\text{core}} & r = R_1 \\ T_{\text{space}} & r = R_2 \\ T_0 & \text{otherwise} \end{cases} \tag{4.1.13}$$

For the second initial profile, we prescribe an anomaly $T_{\text{space}} - 0.05\Delta T$ in the point $(r, \theta) = ((R_2 - R_1)/2, \pi/2)$. Thus, the profile is symmetric. The last initial profile is asymmetric with the anomaly placed in $(r, \theta) = ((R_2 - R_1)/2, \pi/4)$.

4.1.2   Algorithm

The key step to obtaining a quartet $(\vec{v}, \pi, T, h) \in \mathbb{R}^2 \times \mathbb{R} \times \mathbb{R} \times \mathbb{R}$, which solves the approximate problem, is to decouple the system in time, i.e., to seek the solution to Stokes problem $(\vec{v}, \pi)$ and the solution to heat equation T and advection equations h on two different consecutive time levels. The decoupling leads to the following solution-seeking algorithm (see also Fig. 4.1):

0: Let the temperature T^n and surface position h^n be known on the n-th time level, i.e., solutions $T(r, \theta, t)$, $h(\theta, t)$ are known at the fixed time $t = n\Delta t$ where Δt is the time step.

1: Using T^n, h^n define density, viscosity and volume forces in Ω by eqs. (4.1.4), (4.1.5), (4.1.6).

2: Solve the Stokes problem (eqs. (4.1.1), (4.1.2)). Since Stokes problem is stationary, the solution $(\vec{v}^n, \pi^n)$ remains on the n-th time level.

3: Using the computed velocity field, solve the heat equation (eq. (4.1.3)) to obtain temperature field at $n + 1$-th time level.

4: Using the computed velocity field, solve the advection equation (eq. (4.1.8)) to obtain the surface height at $n + 1$-th time level.

5: With T^{n+1}, h^{n+1} goto step 1.

Due to simplifications of our model and consequently the approximate problem, the first step of the algorithm is trivial. However, the remaining steps are quite intriguing and must be solved carefully. We present our methods of obtaining numerical solutions to appropriate partial differential equations from steps 2., 3., 4., in the next sections.
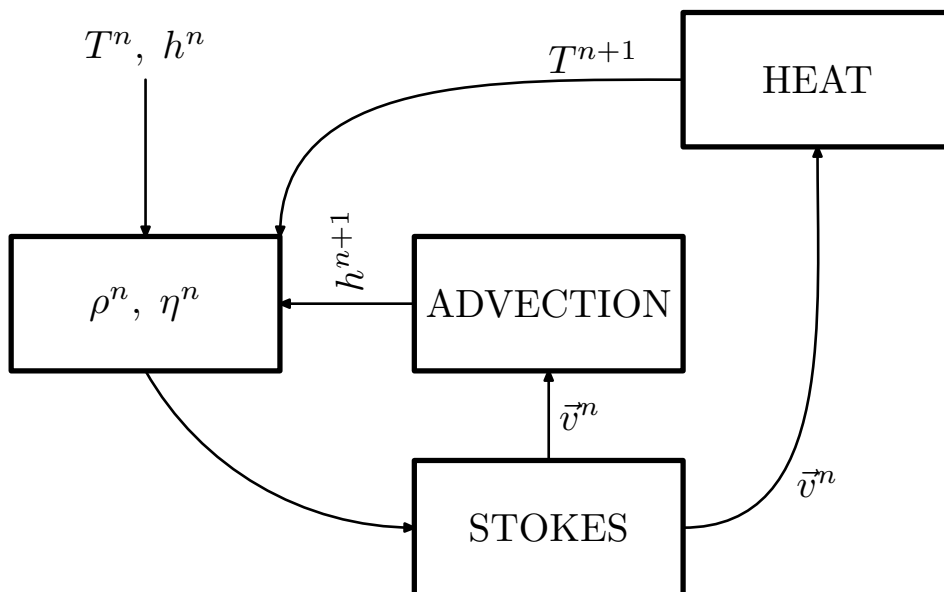
Figure 4.1: Flowchart for algorithm used to solve the approximate problem.

4.2 Stokes problem

The Stokes problem of decoupled approximate problem takes the form

$$\nabla \cdot \vec{v}^n = 0,$$
$$-\nabla \pi^n + \nabla \cdot \left(\eta^n \left(\nabla \vec{v}^n + (\nabla \vec{v}^n)^{\mathrm{T}} \right) \right) + \rho^n \vec{f}^n = 0,$$

where for general (scalar/vector valued) function $\varphi(\vec{x}, t)$ we denote φ^n its projection to n-th time level, that is, $\varphi^n = \varphi(\bullet, n\Delta t)$. For better readability, we drop the superscript as the equations include only spatial derivatives of the projections to same time level. We express the system in polar coordinates (Appendix A) and apply conservative finite-difference method on staggered grid.

Conservative FDM guarantee the conservation of stresses. Due to variable viscosity, the stresses would not be conserved if non-conservative FDM were used.

Staggered grid consists of different types of nodes that are used to define different quantities. The types of nodes are shown in Fig. 4.2. Consequently it is more convenient to differentiate particular equation in certain type of node than in others. We choose to differentiate the continuity equation in pressure nodes, the momentum equation in direction $\vec{e}_r$ in radial velocity nodes and finally, the momentum equation in direction $\vec{e}_\theta$ in tangential velocity nodes.

Differentiating a partial differential equation in the point $(r_i, \theta_j) = (i\Delta r, j\Delta \theta)$, which we denote as (i, j), of the staggered grid with fixed radial and angular step sizes Δr, $\Delta \theta$ leads to a finite difference equation defined on a finite set of nodes. Usually, the FDE takes the form

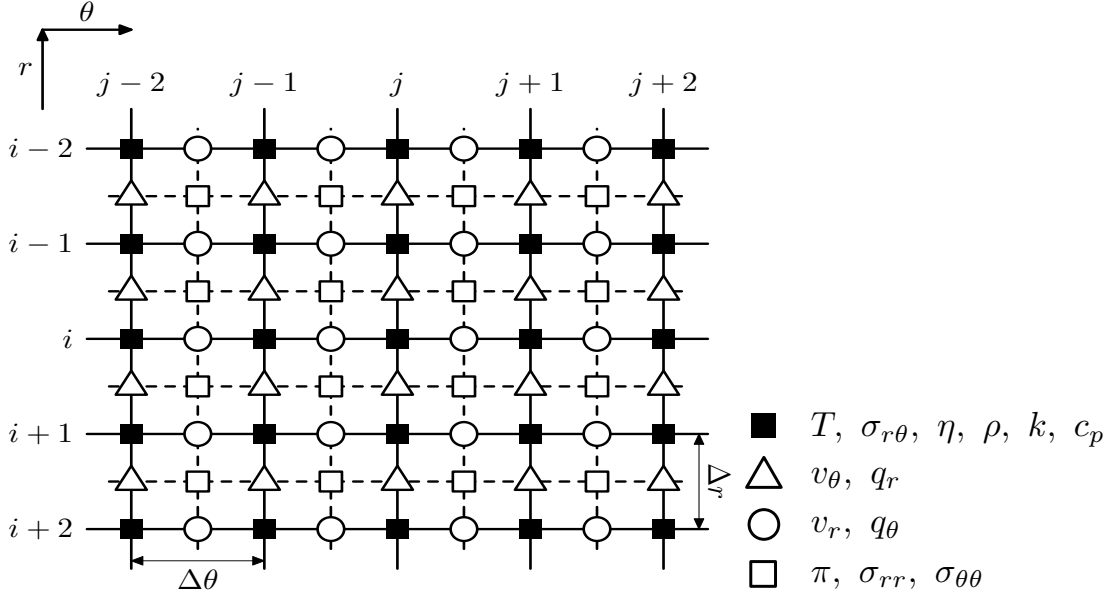$$\vec{W}(i, j) \cdot \vec{V}(i, j) = F(i, j), \tag{4.2.1}$$

Figure 4.2: Staggered grid in polar coordinates (Fig. borrowed from (Běhounková, 2007) and modified). We zoom on a small part of a very dense curvilinear grid so that it can be viewed as regular. Different quantities are defined in different nodes. In full black squares we define material properties, temperature and shear component of deviatoric stress. In empty white triangles we define tangential velocities and radial heat flux. In empty white circles we define radial velocities and tangential heat flux. In empty white square we define pressure and normal deviatoric stresses.

where $\vec{V}(i,j) \in \mathbb{R}^d$ is a vector of nodal values used to approximate the original PDE differentiated in point (i,j), d is the number of nodes, $\vec{W}(i,j) \in \mathbb{R}^d$ is the vector of corresponding weights and $F(i,j) \in \mathbb{R}$ is the discrete value of the right hand side. For example, the continuity equation discretized in point $(i+1, j+1)$ has the right-hand-side $F(i,j)$ equal to zero and vectors $\vec{V}(i+1, j+1)$ and $\vec{W}(i+1, j+1)$ have the following components

$$\vec{V}(i+1, j+1) = \left(v_{r,(i,j+1)}, v_{r,(i+2,j+1)}, v_{\theta,(i+1,j+2)}, v_{\theta,(i+1,j)} \right),$$
$$\vec{W}(i+1, j+1) = \left(\frac{r_i^2}{2r_{i+1}^2 \Delta r}, -\frac{r_{i+2}^2}{2r_{i+1}^2 \Delta r}, \frac{\sin \theta_{j+2}}{r_{i+1} \sin \theta_{j+1}}, -\frac{\sin \theta_j}{r_{i+1} \sin \theta_{j+1}} \right),$$

where for function $\phi(r, \theta)$ nodal value $\phi_{(i,j)}$ is defined as $\phi(i\Delta r, j\Delta\theta)$. Vectors for the two remaining equations of Stokes problem can be found in Appendix B.

If the solution $(\vec{v}, \pi)$ of Stokes problem is sufficiently smooth $((\pi, \vec{v}) \in C^2(\overline{\Omega}) \times C^3(\overline{\Omega})^2)$ and we restrict ourselves to nodes away from the region with density and viscosity discontinuity, it can be shown by means of Taylor's theorem, that each finite difference approximation is of second order of accuracy. In other words, the solution of the differential system satisfies the difference system with error $O([\Delta r]^2, [\Delta\theta]^2)$.

Because of the boundary conditions of Stokes problem, the pressure solution is given up to an arbitrary constant. Consequently, matrix of the finite difference system is ill-

conditioned. A common way of determining the constant is to prescribe the value of pressure in one node. In (Kuchta, 2008) the problem is treated by penalization/allowing small compressibility in continuity equation. Much to our surprise, by using direct solver implemented in UMFPACK we are able to invert the matrix without allowing compressibility or setting the pressure. We offer a summary of our *trick* and discuss what we believe is the key to its success.

UMFPACK inversion has two stages. After the first symbolic stage, where information about the matrix structure is gathered, a numerical stage follows where the values of entries are used and the matrix is actually inverted. We assume that our *trick* successfully abuses this two stage algorithm. For the symbolic stage we provide the solver with discretized continuity equation that indicates compressibility, i.e., FD approximation to $\nabla \cdot \vec{v} + \epsilon \pi = 0$. However, for the numerical stage we set $\epsilon = 0$. UMFPACK is then able to solve our system. Interestingly enough, the inversion requires less time than the inversion of system with nonzero compressibility.

4.3   Heat equation

The heat equation of the decoupled approximate problem discretized semi-implicitly[1] in time takes the form

$$\rho_{0,\text{ice}} C_p \Big(\frac{T^{n+1} - T^n}{\Delta t} + \vec{v}^n \cdot \nabla T^{n+1} \Big) = \nabla \cdot \big(k \nabla T^{n+1} \big), \qquad (4.3.1)$$

where $T^n = T^n(\vec{x}) = T(\vec{x}, n\Delta t)$ retains its meaning from the previous section. The velocity field $\vec{v}^n$ is known from the solution of Stokes problem. This equation can be simplified by taking advantage of the fact that conductivity is constant. Expressing the equation in polar coordinates leads to

$$\frac{T^{n+1} - T^n}{\Delta t} = \Big(2\frac{\kappa}{r} - v_r^n \Big) \frac{\partial T^{n+1}}{\partial r} + \kappa \frac{\partial^2 T^{n+1}}{\partial r^2} + \Big(\frac{\kappa \cos\theta}{r^2 \sin\theta} - \frac{v_\theta^n}{r} \Big) \frac{\partial T^{n+1}}{\partial \theta} + \frac{\kappa}{r^2} \frac{\partial^2 T^{n+1}}{\partial \theta^2}.$$
$$(4.3.2)$$

Equation (4.3.2) is differentiated on the staggered grid (Fig. 4.2) using two non-conservative finite difference schemes. There is no need for conservative FDM as the conservation of heat fluxes is given due to constant conductivity.

4.3.1   Scheme of Crank and Nicolson

The Crank-Nicolson method defines the finite difference approximation of eq. (4.3.2) as

$$\frac{T^{n+1} - T^n}{\Delta t} = \Big[(\boldsymbol{A}^n + \boldsymbol{B} + \boldsymbol{C}^n + \boldsymbol{D}) \Big(\frac{T^{n+1} + T^n}{2} \Big) \Big], \qquad (4.3.3)$$

---

[1]Discretization is semi-implicit because of the term $\vec{v}^n \cdot \nabla T^{n+1}$.

where the difference operators are defined in the following way

$$\left(\boldsymbol{A}^k T^l\right)_{(i,j)} = a_{(i,j)}^k \frac{T_{(i+1,j)}^l - T_{(i-1,j)}^l}{2\Delta r}, \ a_{(i,j)}^k = \left(2\frac{\kappa}{r_i} - v_{r,(i,j)}^k\right) \in \mathbb{R}$$

$$\left(\boldsymbol{B} T^l\right)_{(i,j)} = b_{(i,j)} \frac{T_{(i+1,j)}^l - 2T_{(i,j)}^l + T_{(i-1,j)}^l}{(\Delta r)^2}, \ b_{(i,j)} = \kappa \in \mathbb{R}^+$$

$$\left(\boldsymbol{C}^k T^l\right)_{(i,j)} = c_{(i,j)}^k \frac{T_{(i,j+1)}^l - T_{(i,j-1)}^l}{2\Delta\theta}, \ c_{(i,j)}^k = \left(\frac{\kappa\cos\theta_j}{r_i^2\sin\theta_j} - \frac{v_{\theta,(i,j)}^k}{r_i}\right) \in \mathbb{R}$$

$$\left(\boldsymbol{D} T^l\right)_{(i,j)} = d_{(i,j)} \frac{T_{(i,j+1)}^l - 2T_{(i,j)}^l + T_{(i,j-1)}^l}{(\Delta\theta)^2}, \ d_{(i,j)} = \left(\frac{\kappa}{r_i^2}\right) \in \mathbb{R}^+$$

For function $\varphi(r, \theta, t)$ we define its nodal value $\varphi_{(i,j)}^n$ as $\varphi(i\Delta r, j\Delta\theta, n\Delta t)$. If the solution to eq. (4.1.3) is $T \in C^1([0, T]) \times C^3(\overline{\Omega})$ and we plug it into the difference scheme the original equation can be recovered with error that is $O(\Delta t, [\Delta r]^2, [\Delta\theta]^2)$. Thus, the scheme is first order accurate in time and second order accurate in space.

Consistency of the scheme does not imply that the exact solution of the difference equation converges to the exact solution of the differential equation as grid is made finer. Convergence is often studied using results of Lax and Richtmyer (e.g., Strikwerda (2004)).

Theorem 4.3.1. (The Lax-Richtmyer Equivalence Theorem) *A consistent one-step scheme for a well-posed initial value problem for partial differential equation is convergent if and only if it is stable.*

Since the original theorem is not concerned with initial-boundary-value problems, Fletcher (1991) suggests that it cannot be applied rigorously and should be interpreted as providing necessary but not always sufficient conditions. On the other hand, the theorem is often used for various linear problems in a form *Consistency+Stability=Convergence*. Regardless of form of the theorem applied, stability of the scheme should be investigated.

Stability

We investigate the stability by von Neumann method (e.g., Richtmyer and Morton (1967)). The method is used for stability analysis of schemes for problems with constant coefficients but according to Strikwerda (2004), it can also be applied to problems with variable coefficients.

He argues that global instability is caused by local instabilities that are not dampened. Consequently, stability of the scheme for problem with variable coefficients is determined by local stability. When investigating local stability, the values of coefficients are frozen. Thus, constant coefficients problem is investigated and von Neumann stability analysis can be used. If each of the frozen coefficients problems arising from the scheme is stable, then the variable coefficients problem is also stable.

Our aim to show that the Crank-Nicolson scheme for eq. (4.3.2) is unconditionally stable.

Lemma 4.3.2. *The scheme defined by eq. (4.3.3) is unconditionally stable.*

Proof. Let us choose a node (r, q) from the interior of Ω and set the coefficients constant in such a way that $a_{(i,j)}^k = a_{(r,q)}^k$, $b_{(i,j)} = b_{(r,q)}$, $c_{(i,j)}^k = c_{(r,q)}^k$, $d_{(i,j)} = d_{(r,q)} \, \forall (i,j)$. We apply the von Neumann method to problem with constant coefficients and seek the solution as

$$T_{(i,j)}^n = \lambda^n \exp(\imath k_r \Delta r) \exp(\imath k_\theta \Delta \theta),$$

where k_r, k_θ are components of the wave vector and λ is the amplification factor. Here we consider our grid to be Cartesian as in Fig. 4.2. We propose that this approximation is reasonable, if the grid is dense and improves as the grid is made finer.

Substituting the ansatz into difference equation, we obtain

$$\frac{\lambda^{n+1} - \lambda^n}{\Delta t} = a\lambda^{n+1}\frac{\imath \sin \phi}{2\Delta r} + a\lambda^n \frac{\imath \sin \phi}{2\Delta r} + c\lambda^{n+1}\frac{\imath \sin \varphi}{2\Delta \theta} + c\lambda^n \frac{\imath \sin \varphi}{2\Delta \theta}$$
$$- b\lambda^{n+1}\frac{2\sin^2 \phi/2}{(\Delta r)^2} - b\lambda^n \frac{2\sin^2 \phi/2}{(\Delta r)^2} - d\lambda^{n+1}\frac{2\sin^2 \varphi/2}{(\Delta \theta)^2} - d\lambda^n \frac{2\sin^2 \varphi/2}{(\Delta \theta)^2},$$

where $\phi = k_r \Delta r$, $\varphi = k_\theta \Delta \theta$ and a, b, c, d are the frozen coefficients. The amplification factor is then given as

$$\lambda = \frac{1 - \psi + \imath \xi}{1 + \psi - \imath \xi},$$

where for better readability we set

$$\psi = b\Delta t \frac{2\sin^2 \phi/2}{(\Delta r)^2} + d\Delta t \frac{2\sin^2 \varphi/2}{(\Delta \theta)^2}, \qquad \xi = a\Delta t \frac{\sin \phi}{2\Delta r} + c\Delta t \frac{\sin \varphi}{2\Delta \theta}.$$

According to von Neumann definition of stability (e.g., Richtmyer and Morton (1967)), the necessary and sufficient condition for stability is that the amplification factor is bounded

$$|\lambda|^2 \leq 1 + O(\Delta t).$$

Since in our case $\psi > 0$, we get

$$|\lambda|^2 = \frac{(1 - \psi)^2 + \xi^2}{(1 + \psi)^2 + \xi^2} = 1 - \frac{4\psi}{(1 + \psi)^2 + \xi^2} \leq 1.$$

This proves unconditional stability of the scheme for problem with constant coefficients determined by (r, q). The only requirement that we used was that ψ is positive but this is guaranteed in whole Ω, i.e., independent of (r, q). Therefore, unconditional stability holds for all values of coefficients. Finally, using argument due to Strikwerda (2004) we obtain unconditional global stability. $\square$

Remark: In our proof we dropped the subscript indicating time levels from a^n, c^n and consequently ξ^n, ψ^n, λ^n. If retained, we would obtain sequence of amplification factors $\{\lambda^n\}$, with every member $|\lambda^n|^2 \leq 1$. Thus, the instabilities would not be amplified between any two consecutive time levels. Consequently, they would not be amplified on some interval. Our conclusion about unconditional stability therefore holds.

4.3.2   Upwind scheme

While the scheme of Crank and Nicolson uses only central differences to approximate spatial derivatives, the upwind scheme chooses between forward and backward differences depending on the sign of coefficients in front of the derivatives. For convenience, we rewrite eq. (4.3.2) in a more suitable form

$$\frac{T^{n+1} - T^n}{\Delta t} = 2\frac{\kappa}{r}\frac{\partial T^{n+1}}{\partial r} + \kappa\frac{\partial^2 T^{n+1}}{\partial r^2} + \frac{\kappa\cos\theta}{r^2\sin\theta}\frac{\partial T^{n+1}}{\partial\theta} + \frac{\kappa}{r^2}\frac{\partial^2 T^{n+1}}{\partial\theta^2}$$
$$- v_r\frac{\partial T^{n+1}}{\partial r} - \frac{v_\theta}{r}\frac{\partial T^{n+1}}{\partial\theta}. \tag{4.3.4}$$

We apply upwinding only to the convective term. The implicit upwind scheme defines approximation to eq. (4.3.4) as

$$\frac{T^{n+1} - T^n}{\Delta t} = \left[\left(\boldsymbol{A} + \boldsymbol{B} + \boldsymbol{C} + \boldsymbol{D} + \boldsymbol{E}^n + \boldsymbol{F}^n\right)T^{n+1}\right], \tag{4.3.5}$$

where the difference operators are defined in the following way

$$\left(\boldsymbol{A}T^l\right)_{(i,j)} = a_{(i,j)}\frac{T^l_{(i+1,j)} - T^l_{(i-1,j)}}{2\Delta r}, \ a^k_{(i,j)} = 2\frac{\kappa}{r_i} \in \mathbb{R}^+$$

$$\left(\boldsymbol{B}T^l\right)_{(i,j)} = b_{(i,j)}\frac{T^l_{(i+1,j)} - 2T^l_{(i,j)} + T^l_{(i-1,j)}}{(\Delta r)^2}, \ b_{(i,j)} = \kappa \in \mathbb{R}^+$$

$$\left(\boldsymbol{C}T^l\right)_{(i,j)} = c_{(i,j)}\frac{T^l_{(i,j+1)} - T^l_{(i,j-1)}}{2\Delta\theta}, \ c_{(i,j)} = \frac{\kappa\cos\theta_j}{r_i^2\sin\theta_j} \in \mathbb{R}$$

$$\left(\boldsymbol{D}T^l\right)_{(i,j)} = d_{(i,j)}\frac{T^l_{(i,j+1)} - 2T^l_{(i,j)} + T^l_{(i,j-1)}}{(\Delta\theta)^2}, \ d_{(i,j)} = \left(\frac{\kappa}{r_i^2}\right) \in \mathbb{R}^+$$

$$\left(\boldsymbol{E}^kT^l\right)_{(i,j)} = -\left(v^k_{r,(i,j)}\left(\frac{T^l_{(i+1,j)} - T^l_{(i-1,j)}}{2\Delta r}\right) - |v^k_{r,(i,j)}|\left(\frac{T^l_{(i+1,j)} - 2T^l_{(i,j)} + T^l_{(i-1,j)}}{2\Delta r}\right)\right)$$

$$\left(\boldsymbol{F}^kT^l\right)_{(i,j)} = -\frac{1}{r_i}\left(v^k_{\theta,(i,j)}\left(\frac{T^l_{(i,j+1)} - T^l_{(i,j-1)}}{2\Delta\theta}\right) - |v^k_{\theta,(i,j)}|\left(\frac{T^l_{(i,j+1)} - 2T^l_{(i,j)} + T^l_{(i,j-1)}}{2\Delta\theta}\right)\right)$$

The scheme is first order accurate in time, but unlike scheme of Crank-Nicolson, it is only first order accurate in space. This is caused by the upwinding. On the other hand, upwinding is also responsible for dissipative property of the scheme. In our case, dissipativity is a desirable property as it improves the ability of scheme to dampen unwanted oscillations.

Stability

When subjected to analysis of stability, the implicit scheme with upwinding on convective term for eq. (4.3.4) turns out to be unconditionally stable

Lemma 4.3.3. *The scheme defined by eq. (4.3.5) is unconditionally stable.*

Proof. We follow steps of the proof of unconditional stability of the Crank-Nicolson scheme. The amplification factor is given as

$$\lambda = \frac{1}{1 + \psi - \imath\xi},$$

where

$$\psi = \Delta t \left(\frac{4b}{(\Delta r)^2} + \frac{2|v_{r,(r,q)}^k|}{\Delta r} \right) \sin^2\varphi/2 + \Delta t \left(\frac{4d}{r_r(\Delta\theta)^2} + \frac{2|v_{\theta,(r,q)}^k|}{r_r\Delta\theta} \right) \sin^2\phi/2,$$

$$\xi = \frac{\Delta t}{\Delta r} \left(a - v_{r,(r,q)}^k \right) \sin\varphi + \frac{\Delta t}{\Delta\theta} \left(c - v_{r,(r,q)}^\theta \right) \sin\phi.$$

We can see that $\psi > 0$ and thus

$$|\lambda|^2 = \frac{1}{(1 + \psi)^2 + \xi^2} \leq 1.$$

$\square$

4.4   Advection of surface

Evolution of surface is defined by initial-value problem (4.1.8). The approximation of the problem by semi-implicit upwind scheme is written as

$$\left.\begin{array}{r} \dfrac{h^{n+1} - h^n}{\Delta t} + \boldsymbol{A}^n h^{n+1} = \tilde{V}_r^{\ n} \\[2mm] h^0 \text{ given} \end{array}\right\}, \tag{4.4.1}$$

where h^0 is the discretized initial condition h_0. Components of vector $\tilde{V}_r^{\ n} = (\tilde{v}_{r,m}^n)_{m=0}^M$, $M\Delta\theta = \pi$ are constructed by extrapolation from nodal values of radial velocity field at time level n to points $\theta_m = m\Delta\theta$. Used nodes must lie in ice region. The difference operator $\boldsymbol{A}^k$ is given as

$$(A^k h^l)_m = a_m^k \frac{h_{m+1}^l - h_{m-1}^l}{2\Delta\theta} - |a_m^k| \frac{h_{m+1}^l - 2h_m^l + h_{m-1}^l}{2\Delta\theta}, \ a_m^k = \frac{\tilde{v}_{\theta,m}^n}{r_m}, \tag{4.4.2}$$

where $\tilde{v}_{\theta,m}^n$ are defined from tangential velocity field at time level n in a similar way to $\tilde{v}_{r,m}^n$. The scheme (4.4.1) is first order accurate in both time and space.

Stability

We investigate stability using energy method (e.g., Dautray et al. (2000)). Basic idea of the method is that the conditions under which we can prove that the difference problem is well-posed are the stability conditions of the scheme. Our aim is to prove unconditional stability of the scheme (4.4.1).

Lemma 4.4.1. *The scheme defined by (4.4.1) is unconditionally stable.*

Proof. We divide the proof into three steps. In the first two steps, we consider simplified versions of scheme (4.4.1) and show their unconditional stability. In the final step we use our findings to show unconditional stability of the original scheme.

Step 1: Let us consider difference scheme

$$\left.\begin{array}{c} \dfrac{h^{n+1} - h^n}{\Delta t} + \boldsymbol{A}h^{n+1} = 0 \\[2mm] h^0 \text{ given} \end{array}\right\}, \tag{4.4.3}$$

where

$$(Ah^l)_m = a\frac{h^l_{m+1} - h^l_{m-1}}{2\Delta\theta} - |a|\frac{h^l_{m+1} - 2h^l_m + h^l_{m-1}}{2\Delta\theta}, \; a \in \mathbb{R}.$$

We equip the space l^2 of sequences $g = \{g_m\}$ with scalar product $\langle g, h \rangle = \sum\limits_{m=0}^{M} g_m h_m$ which induces the norm of solution $|h| = (\sum\limits_{m=0}^{M} h_m h_m)^{1/2}$. Squaring the first equation of (4.4.3), we obtain

$$|h^{n+1}|^2 - |h^n|^2 = -2\Delta t \langle \boldsymbol{A}h^{n+1}, h^{n+1} \rangle - (\Delta t)^2 \langle \boldsymbol{A}h^{n+1}, \boldsymbol{A}h^{n+1} \rangle.$$

The first term on the right hand side is nonnegative due to Lemma 1. on p. 103 in Dautray et al. (2000). The second term is obviously nonnegative. Therefore we have

$$|h^{n+1}|^2 - |h^n|^2 \leq 0 \implies |h^{n+1}|^2 \leq |h^n|^2 \implies |h^{n+1}|^2 \leq |h^0|^2.$$

Thus, the difference problem (4.4.3) is well-posed independent of Δt, $\Delta \theta$ or a. Consequently, the scheme is unconditionally stable.

Step 2: Let us consider scheme (4.4.1) with zero right hand side. We use the same procedure as in Step 1. Instead of the result from (Dautray et al., 2000) we use the estimate

$$\langle \boldsymbol{A}^n h^{n+1}, h^{n+1} \rangle \leq \|\boldsymbol{A}^n\| |h^{n+1}|^2,$$

where $\|\boldsymbol{A}^n\| = \max\limits_m \{|a^n_m|\}$. It is then possible to show that the solution is bounded by initial data.

Step 3: We consider original scheme (4.4.1). Using Duhamel's principle it can be shown that a scheme for inhomogeneous initial-value problem $Pu = f$ is stable if it is stable for homogeneous initial-value problem $Pu = 0$. Application of the Duhamel's principle to findings of Step 2. then concludes our proof. $\qquad\square$

Chapter 5

Results

In this chapter our numerical method described in Chapter 4 is subjected to tests. We begin by modeling thermal convection in solid spherical shell. In the next test we model viscous relaxation. Finally, in the last tests thermal convection with free surface is modeled.

Preliminaries

The fixed parameters that are shared between the test cases are listed in Table 5.1. The parameters are relicts from the early development stages of our program and they generally do not agree with parameters of Iapetus or water ice. Among other characteristics, the simulations also differ by their thermal Rayleigh number which is defined as

$$Ra = \frac{\Delta T d^3 \rho_{0,\text{ice}}^2 C_p \alpha g_0}{\eta_{0,\text{ice}} k},$$

where $d = R_2 - R_1$, $\Delta T = T_{\text{core}} - T_{\text{space}}$ and $g_0 = (4/3)G\rho_{0,\text{ice}}R_2$ is the surface gravity of our model satellite. This dimensionless number is the sole parameter that determines the nature of thermal convection. Therefore our somewhat unfortunate choice of parameters is irrelevant as long as the results are compared with the model that has the same Ra. We vary the Rayleigh number only by setting different reference viscosity. Some results include dimensionless time $t' = \frac{d^2 \rho_{0,\text{ice}} C_p}{k} t$.

Quantity	Value in SI	Quantity	Value in SI
R_1	$400\,\text{km}$	$\rho_{0,\text{ice}}$	$600\,\text{kg.m}^{-3}$
R_2	$800\,\text{km}$	α	$50 \times 10^{-5}\,\text{K}^{-1}$
T_{space}	$90\,\text{K}$	k	$2.4\,\text{W.m}^{-1}.\text{k}^{-1}$
T_{core}	$3000\,\text{K}$	C_p	$1000\,\text{J.K}^{-1}.\text{kg}^{-1}$
T_0	$273\,\text{K}$	$\rho_{0,\text{air}}$	$10^{-2}\,\text{kg.m}^{-3}$

Table 5.1: Settings of parameters common for all tests.

5.1   Thermal convection with solid surface

Description

In the first test, we study thermal convection in solid spherical shell using Implicit Upwind scheme and Crank-Nicolson scheme to approximate the heat equation. For this purpose the entire computational domain Ω is filled with ice medium and we set $\eta_{0,\text{ice}} = 10^{18}$ Pa.s or $\eta_{0,\text{ice}} = 10^{17}$ Pa.s to obtain different vigor of convection. Boundary conditions follow Chapter 4. We use temperature profile given by eq. (4.1.12) as an initial condition. The time step as well as spatial steps are fixed at $\Delta t = 5.10^4$ yr ($\sim 4.10^{-5}$), $\Delta r \sim 2.4$ km ($\sim 6.10^{-3}$), $R_2 \Delta \theta \sim 1.6$ km ($\sim 2.10^{-3}$).

Our primary aim is to qualitatively compare the nature of convection with results of Moser (1991) where models with similar Rayleigh numbers and initial conditions are studied. In order to characterize convection we define the surface Nusselt number as

$$Nu = -\frac{(R_2 - R_1)^2}{2R_2 R_1} \int_0^\pi \frac{\partial T}{\partial r} \sin \theta \mathrm{d}\theta.$$

Our secondary aim is to compare the numerical schemes and identify the one that is safer to use with more complex models that include free surface.

Results

The nature of convection for models that were considered in this test is compared in Fig. 5.2. We can see that the solution to model with $Ra = 2.10^5$ reaches a quasi-stationary state, while the solution to model with $Ra = 2.10^6$ is chaotic. In Fig. 5.1 the snapshots of temperatures fields are shown at time $t \sim 822$ Myr (0.65). We can see that the solution for $Ra = 2.10^5$ is symmetric. In fact the symmetry is not broken throughout the whole simulation. On the other hand the symmetry is broken in the solution for $Ra = 2.10^6$. These results qualitatively agree with Moser (1991). The author observed quasi-periodic character of solution for $Ra = 10^5$. His solution for $Ra = 5.10^6$ was chaotic in nature, which he attributed to the solution being close to transition to hard turbulence. However the solution for $Ra = 10^6$ remained symmetric. Thus, we conclude that the critical value for break-up of the symmetry lies between $Ra = 1.10^6$ and $Ra = 2.10^6$.

Temperature fields for model with $Ra = 2.10^6$ and time dependences of Nusselt number for model with $Ra = 2.10^5$ reveal most about the differences between Implicit Upwind scheme and scheme of Crank-Nicolson. The temperature profiles show that the model computed with Crank-Nicolson scheme is colder and due to zero dissipativity of the scheme, includes finer thermal formations. Dissipative nature of Implicit Upwind scheme can also be seen in Fig. 5.2 where the amplitudes are smaller compared to C-N scheme. We believe that the difference in dissipativity is also responsible for slight shift in the graphs. In Fig. 5.1 we can see that the C-N solution is colder than $T = 0$, a phenomenon that should not occur as the maximum principle holds for our approximate problem. Even though the scheme prevents propagation of this instability, the Implicit Upwind scheme appears to be more robust. Therefore, in the tests with thermal convection and free surface we decide to use Implicit Upwind scheme.

$Ra = 2.10^5$ $Ra = 2.10^5$

scheme IU, $t' = 0.65$ *scheme CN*, $t' = 0.65$

$Ra = 2.10^6$ $Ra = 2.10^6$

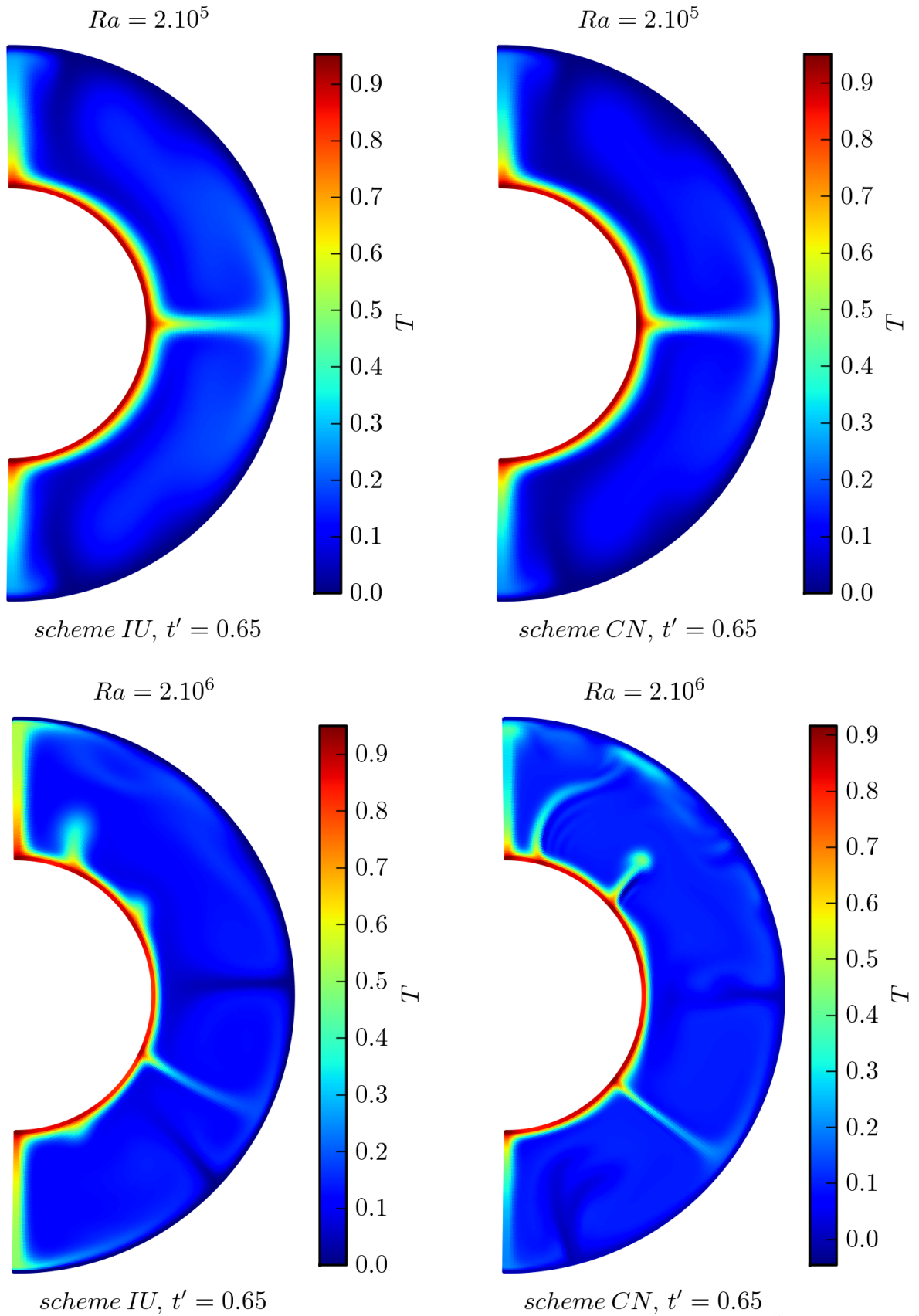*scheme IU*, $t' = 0.65$ *scheme CN*, $t' = 0.65$

Figure 5.1: Comparison of temperature fields at $t' = 0.65$ for $Ra = 2.10^5$, $Ra = 2.10^6$ computed with Implicit Upwind scheme and Crank-Nicolson scheme.
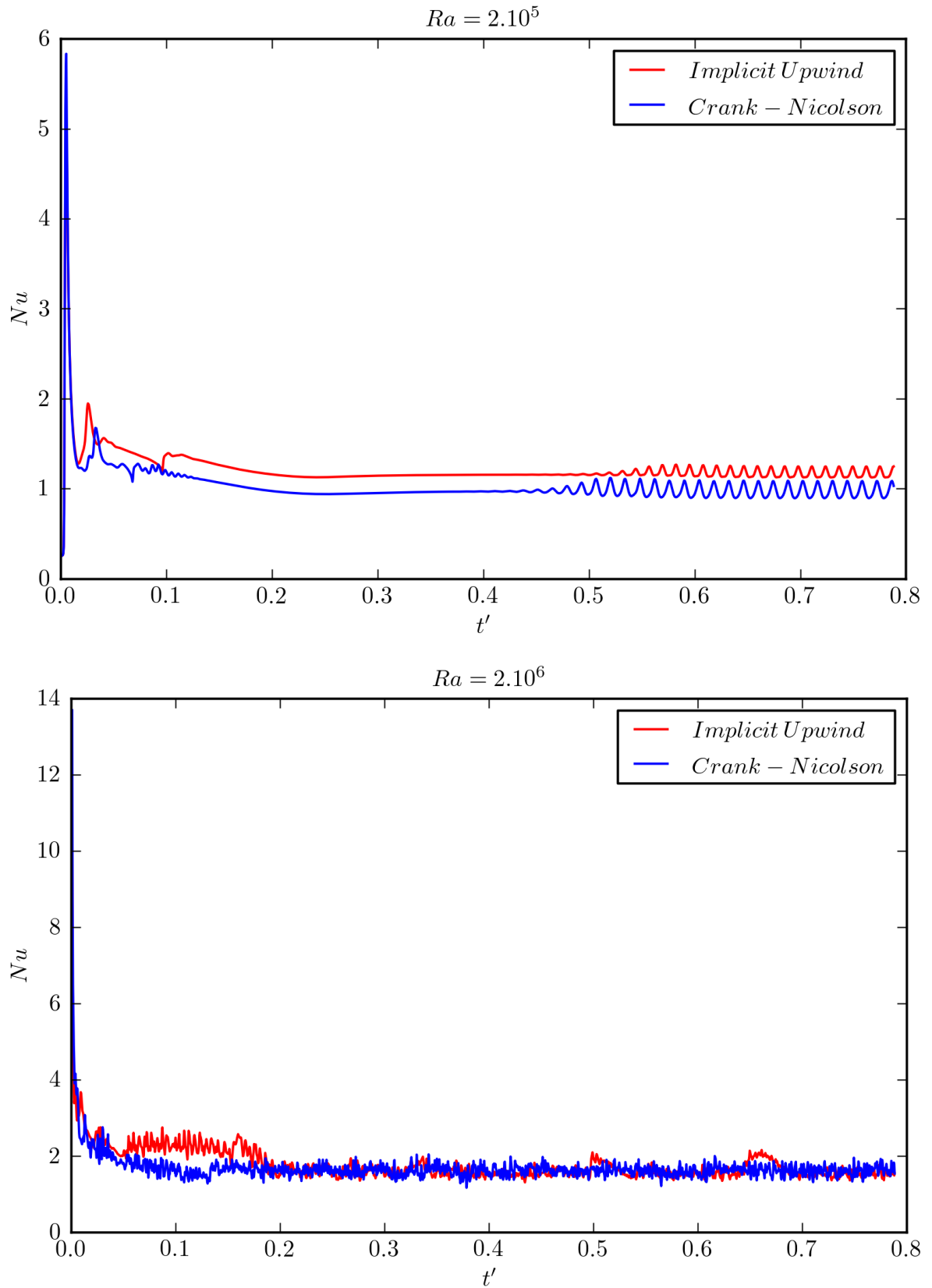
Figure 5.2: Time dependence of Nusselt number for models with $Ra = 2.10^5$, $Ra = 2.10^6$ computed with Implicit Upwind scheme and Crank-Nicolson scheme is compared.

5.2 Viscous relaxation

Description

Having tested the ability of our numerical method to model thermal convection, we now focus on its surface tracking abilities. For this purpose, we consider a model planet that is no longer thermally active and is subjected to gravitational and centrifugal force. Thus, density and material properties in our model do not depend on temperature. The centrifugal force corresponds to rotational period $\tau = 20\,\mathrm{h}$. We prescribe the surface as circular-shaped interface between ice and air medium $h_0(\theta)\text{~}756\,\mathrm{km}$. We set ice viscosity as $\eta_{0,\mathrm{ice}} = 5.10^{18}\,\mathrm{Pa.s}$ and air viscosity as $\eta_{0,\mathrm{air}} = 10^{14}\,\mathrm{Pa.s}$. Boundary conditions follow Chapter 4. As in the previous test, time and spatial steps are fixed at $\Delta t = 10^4\,\mathrm{yr}\,(\text{~}8.10^{-6})$, $\Delta r\text{~}1.6\,\mathrm{km}\,(\text{~}4.10^{-3})$, $R_2\Delta\theta\text{~}2.0\,\mathrm{km}\,(\text{~}5.10^{-3})$.

Our aim is to obtain a solution that would be in agreement with the character of centrifugal force which deforms the surface.

Results

The deformed surface at $t = 0.5\,\mathrm{Myr}$ is shown in Fig. 5.3. The shape is retained almost immediately after the start of deformation and then remains constant throughout the simulation. We fit our solution with function $h(\theta) = A\sin^2\theta + B$ where $A = 737.78 \pm 0.02\,\mathrm{km}$ and $A = 26.02 \pm 0.01\,\mathrm{km}$. Thus, the obtained deformation agrees well with the nature of centrifugal force.

5.3 Thermal convection with free surface

Description

In this test we study thermal convection in a rotating model planet with free surface. We consider four model cases. In model I the Rayleigh number $Ra = 2.10^5$ is constant and gravitational force is the only component of the volume force. In model II we add centrifugal force to model I. In model III our planet rotates and viscosity follows Arrhenius law with reference viscosity of ice set as $\eta_{0,\mathrm{ice}} = 10^{19}\,\mathrm{Pa.s}$. Since the dimensionless surface temperature is $T' = 0$, viscosity on the surface is equal to the reference viscosity. Using the value of surface viscosity, we define the surface Rayleigh number. In this case $Ra_S = 2.10^4$. The a_{vis} parameter in Arrhenius law is such that the viscosity contrast between the coldest and hottest spots in ice is $\Delta\eta = 150$. The viscosity of air medium is set as $\eta_{0,\mathrm{ice}} = 10^{14}\,\mathrm{Pa.s}$ allowing for 10^3 viscosity contrast between ice and air. Settings for model IV replicate those of model III but we treat the discontinuity of viscosity near the interface in the same way as the discontinuity of density. In all models, the surface is prescribed as interface at depth $r\text{~}756\,\mathrm{km}$, the centrifugal force (if present) corresponds to rotational period of $\tau = 16\,\mathrm{h}$, the time and spatial steps are fixed at $\Delta t = 10^4\,\mathrm{yr}\,(\text{~}8.10^{-6})$, $\Delta r\text{~}1.62\,\mathrm{km}\,(\text{~}4.10^{-3})$, $R_2\Delta\theta\text{~}1.97\,\mathrm{km}\,(\text{~}5.10^{-3})$ and the boundary conditions follow Chapter 4. The simulations
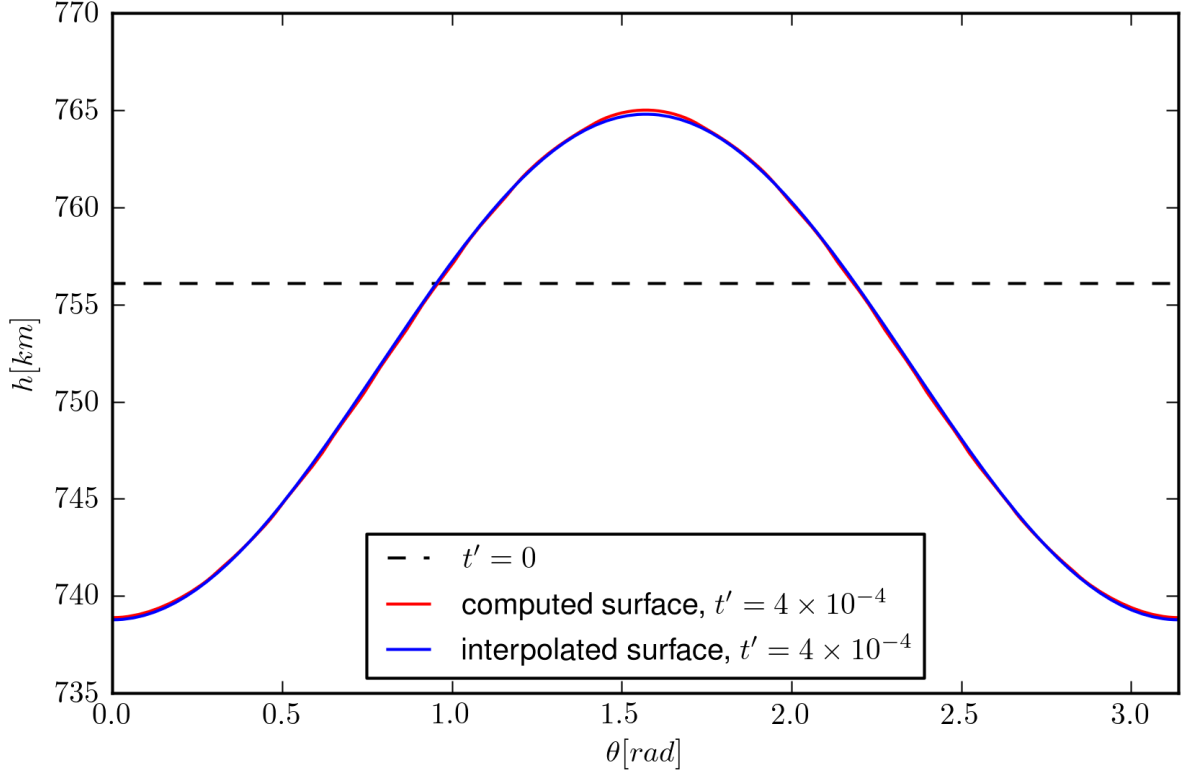
Figure 5.3: Deformed surface of relaxing model planet subjected to gravity and centrifugal force. The shape is fitted with function $h(\theta) = A \sin^2 \theta + B$ to show that it follows the deforming force.

are started from symmetric and asymmetric initial temperature profiles based on eq. (4.1.13) with anomaly $T' = 0.95$.

Our aim is to obtain reasonable surface deformations that can be qualitatively explained by initial conditions, nature of convection and nature of volume forces.

Results for symmetric initial condition

Results for models I-IV started from symmetric initial condition are summarized in Figs. 5.4-5.7. The solutions are symmetric throughout the whole simulation. We can see that the surface shape of model I, where centrifugal force is absent, is determined by rising and falling plumes. In Fig. 5.6, the surface at 17 Myr includes three peaks that correspond to the rising plumes shown at snapshot of temperature field in Fig. 5.4. Figures 5.5 and 5.7 then show that as the northern tropic and southern tropic plumes travel towards the poles, so do the lateral peaks. As the large flattening (~ 25 km) suggests, the surface shape for models II-IV is determined by the centrifugal force. The effect of rising polar plumes is approximately ten times smaller.

It is interesting to compare the temperature fields and surface shapes for models III and IV. With two rising polar plumes in temperature field for model III and an additional rising equatorial plume for model IV, we can see that the character of convection differs significantly between the two models. Consequently, there are also some differences between the surface deformations. However, these differences are relatively small as the shape is predominantly determined by centrifugal force.
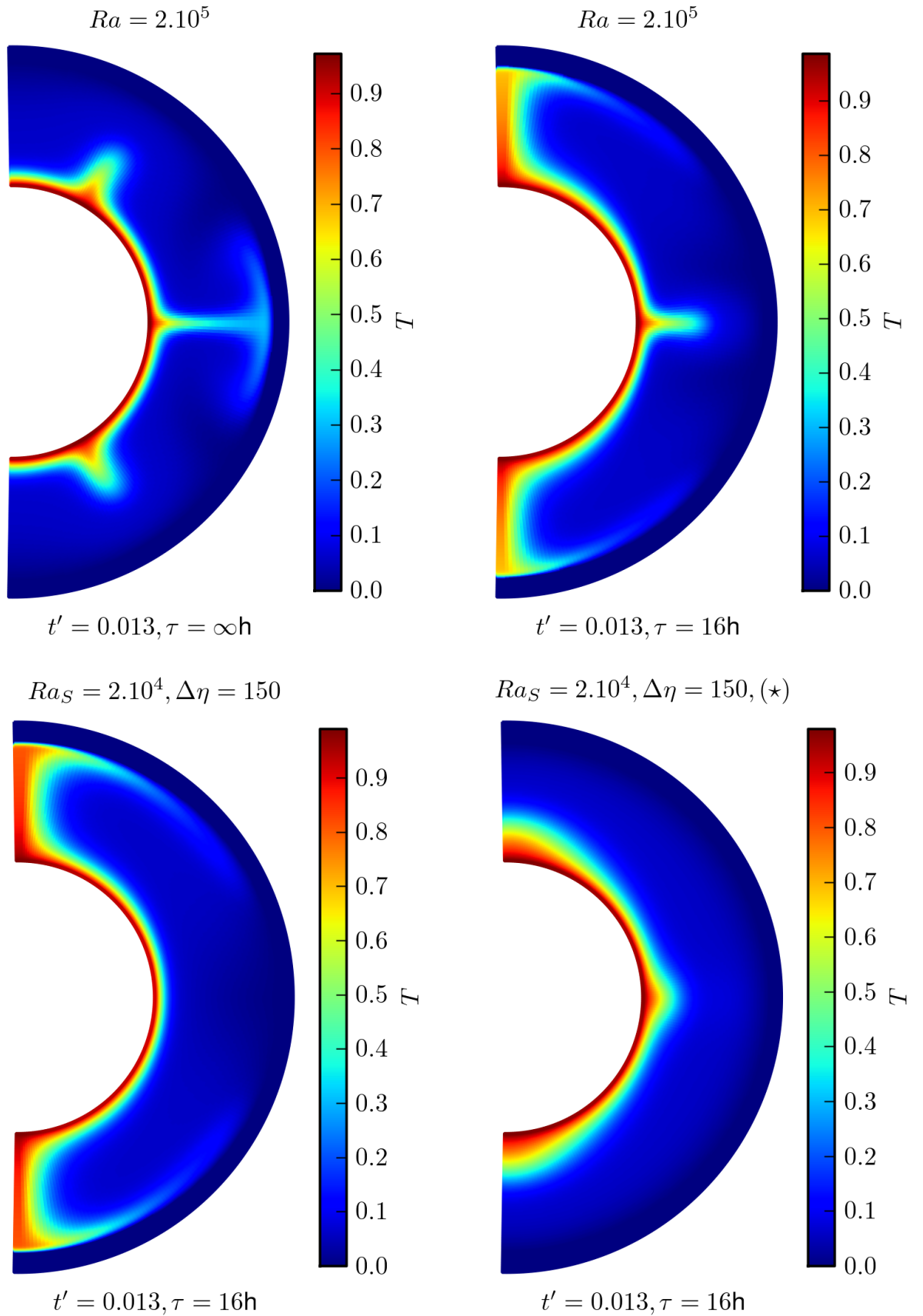
$Ra = 2.10^5$

$t' = 0.013, \tau = \infty \mathsf{h}$

$Ra = 2.10^5$

$t' = 0.013, \tau = 16\mathsf{h}$

$Ra_S = 2.10^4, \Delta\eta = 150$

$t' = 0.013, \tau = 16\mathsf{h}$

$Ra_S = 2.10^4, \Delta\eta = 150, (\star)$

$t' = 0.013, \tau = 16\mathsf{h}$

Figure 5.4: Comparison of temperature fields at $t = 17\,\mathrm{Myr}$ for models I, II, III, IV started from symmetric initial condition. Cold outer layer corresponds to air.
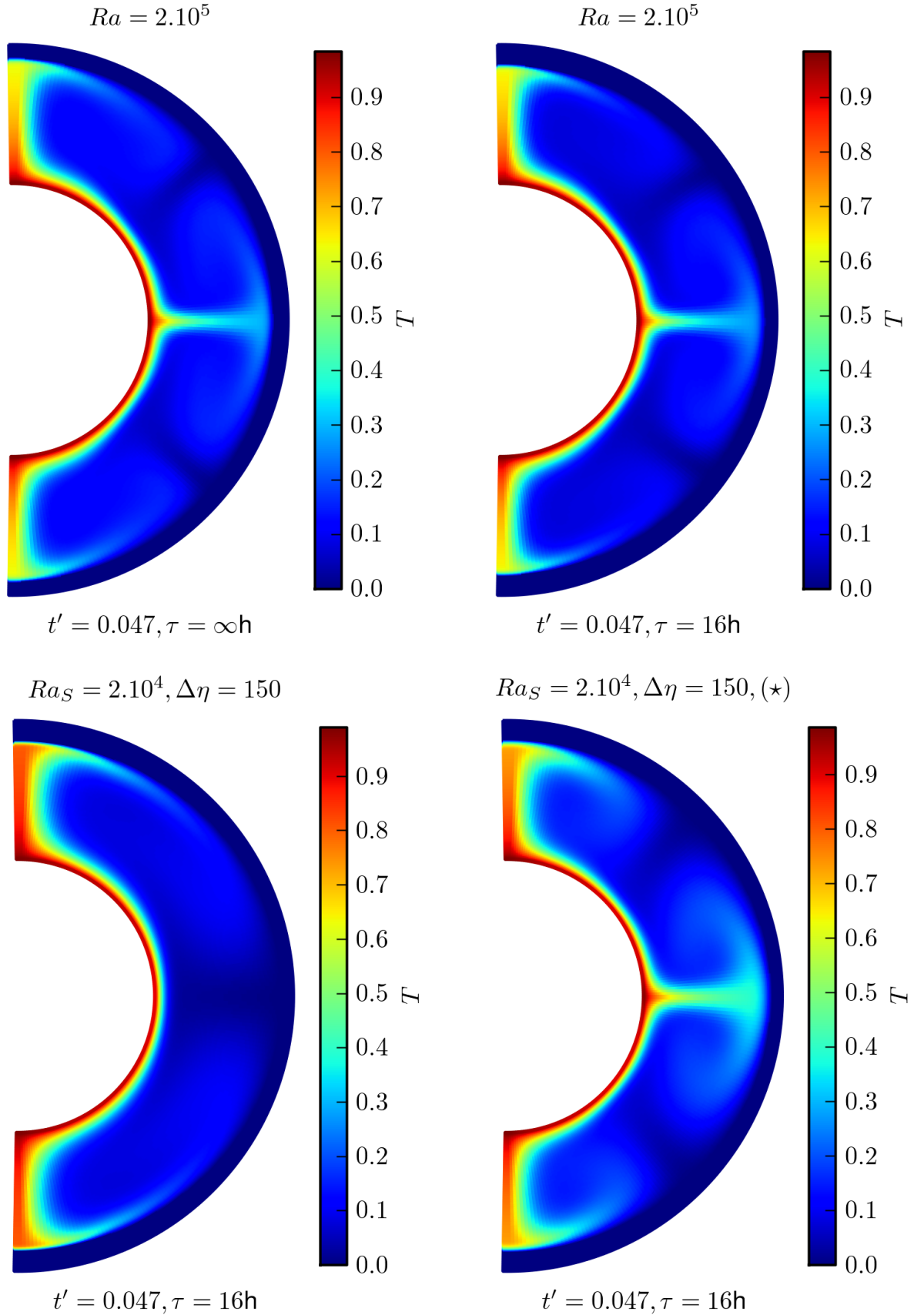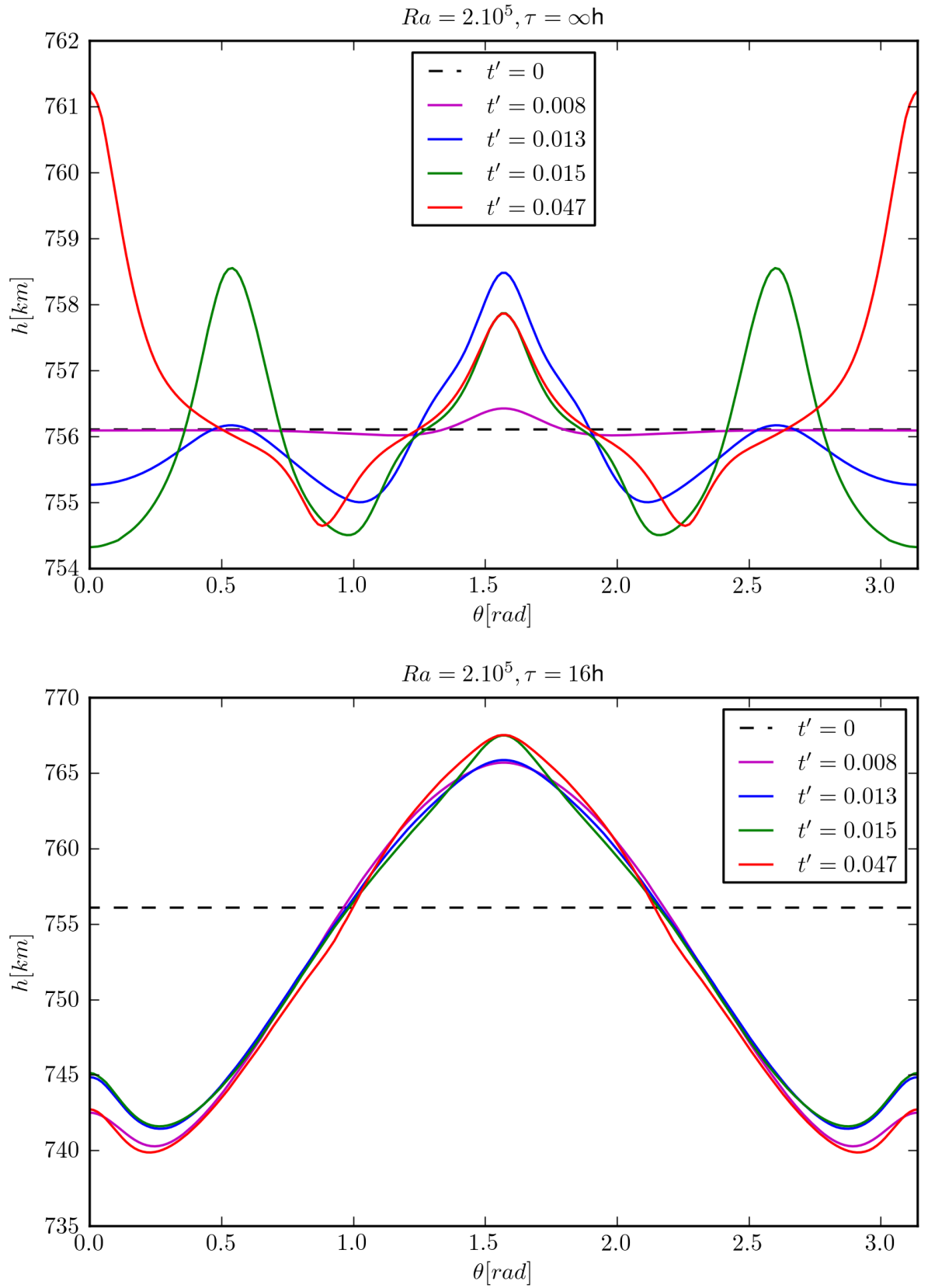
$Ra = 2.10^5$

$Ra = 2.10^5$

$t' = 0.047, \tau = \infty \mathsf{h}$

$t' = 0.047, \tau = 16\mathsf{h}$

$Ra_S = 2.10^4, \Delta\eta = 150$

$Ra_S = 2.10^4, \Delta\eta = 150, (\star)$

$t' = 0.047, \tau = 16\mathsf{h}$

$t' = 0.047, \tau = 16\mathsf{h}$

Figure 5.5: Comparison of temperature fields at $t = 60\,\mathrm{Myr}$ for models I, II, III, IV started from symmetric initial condition. Cold outer layer corresponds to air.

Figure 5.6: Surface evolution for model I and model II started from symmetric initial condition. Snapshots of initial state and states at 10 Myr, 17 Myr,19 Myr and 60 Myr.
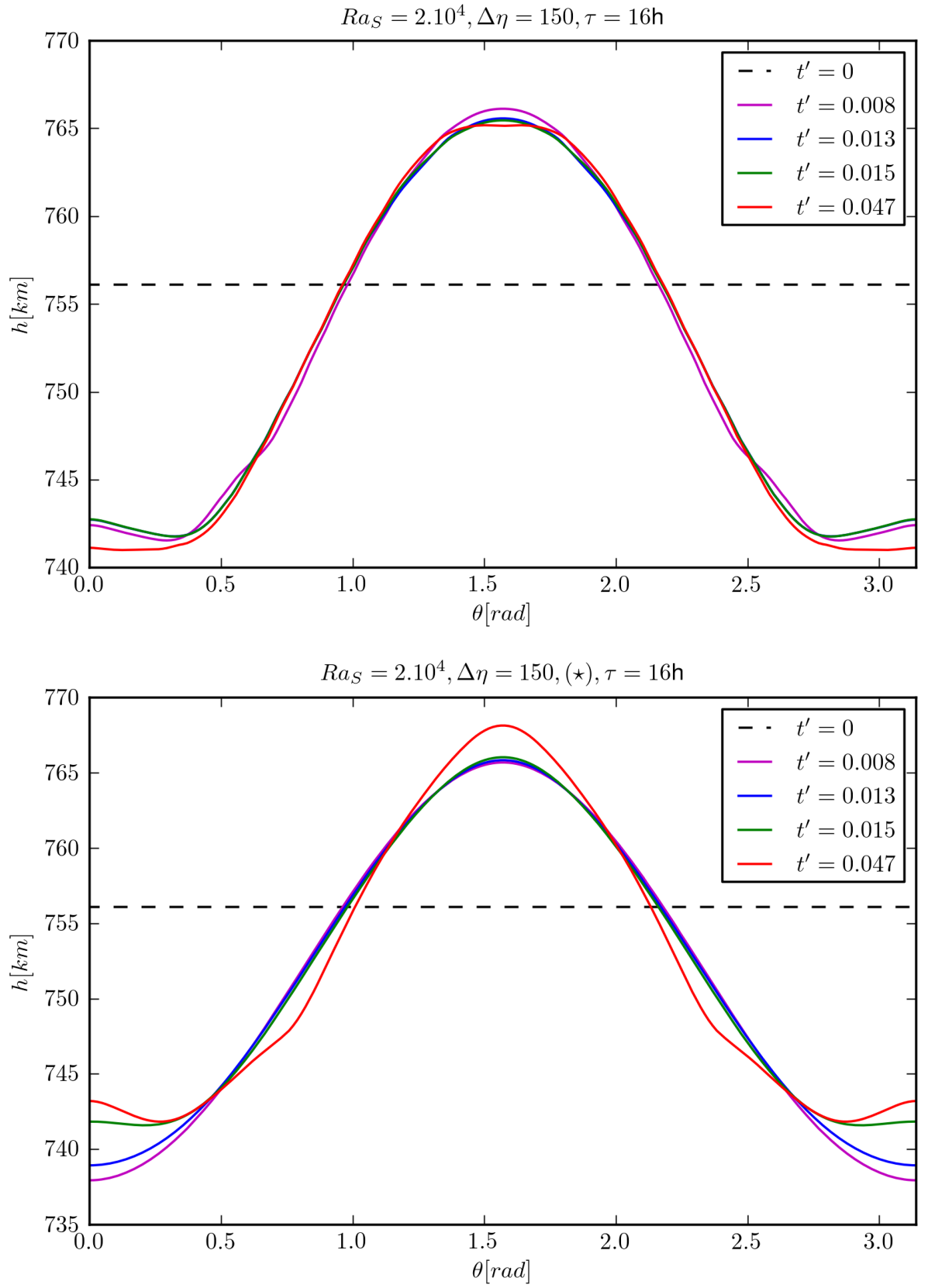
Figure 5.7: Surface evolution for model III and model VI started from symmetric initial condition. Snapshots of initial state and states at 10 Myr, 17 Myr, 19 Myr and 60 Myr.

We believe that onset of the extra plume was caused by instabilities that were introduced into the system by extrapolation of viscosity to air region. The motivation for viscosity smearing was to create a transition zone between ice, where fluid velocities are small, and air, where the flow is vigorous because of very low viscosity. Even though velocities for advection of interface are extrapolated from ice, we fear that the different character of flows could impact our solution especially for models with $Ra_S > 10^6$. In such case regularization of viscosity is a potential treatment but as our test results show, it should be used cautiously.

Results for asymmetric initial condition

Results for models I-IV started from asymmetric initial condition are summarized in Figs. 5.8-5.11. Our conclusions from previous test about the effects that the nature of convection and centrifugal force have on surface shape hold for all models. All deformed surfaces are asymmetric. Because of the absence of centrifugal force, the asymmetry due to thermal anomaly is most apparent in surface deformation of model I (Fig. 5.10). Symmetry of the surface shape for the remaining models appears to be only slightly broken.

In Figs. 5.10 and 5.11 we can see slight oscillations in surface shapes near north pole. Because of the application of polar coordinates, polar axis are most sensitive to numerical errors as there are singular points at $\theta = 0$ and $\theta = \pi$. However, we believe that these oscillations are caused by sudden change of the character of flow. The shape of surface at 10 Myr in Fig. 5.10 corresponds to a cold sinking polar plume (Fig. 5.8). The flow remains stationary for some 80 Myr but at 95 Myr the transition occurs and the plume begins to rise. At 97 Myr the transition is finished; there is a hot rising polar plume in Fig. 5.9. The oscillations are caused by the rapid change of surface area that is due to this rapid change of character of flow.

In Fig. 5.10 we can also notice minor oscillations near $\theta = 1$ and $\theta = 3$. These oscillations usually appear when the gradient of solution is big. Because of the stability of numerical scheme, they do not propagate. The amplitude of oscillations becomes smaller if the grid resolution is improved.

Remark on neglected terms in momentum equation

In Chapter 2 we promised to provide *a posteriori* justification for neglecting inertia from momentum equation of our model. In the first test simulation with $Ra = 2.10^6$, we recorder maximum velocity $U\tilde{} 1 \, \mathrm{m.yr^{-1}}$ and maximum pressure $P\tilde{} 2500 \, \mathrm{Pa}$. We approximate each term in the momentum equation using these maximum values and spatial/time step sizes to obtain the following comparison of magnitudes

$$\frac{\vec{v}_{,t}}{\vec{v} \cdot \nabla \vec{v}} = 10^{-2}, \quad \frac{\vec{v} \cdot \nabla \vec{v}}{\text{pressure gradient}} = 10^{-20}, \quad \frac{\text{pressure gradient}}{\text{divergence of } \boldsymbol{\sigma}} = 10^{-1}$$

Clearly, the inertia can be neglected.

$Ra = 2.10^5$

$t' = 0.016, \tau = \infty \mathsf{h}$

$Ra = 2.10^5$

$t' = 0.016, \tau = 16\mathsf{h}$

$Ra_S = 2.10^4, \Delta\eta = 150$

$t' = 0.016, \tau = 16\mathsf{h}$

$Ra_S = 2.10^4, \Delta\eta = 150, (\star)$
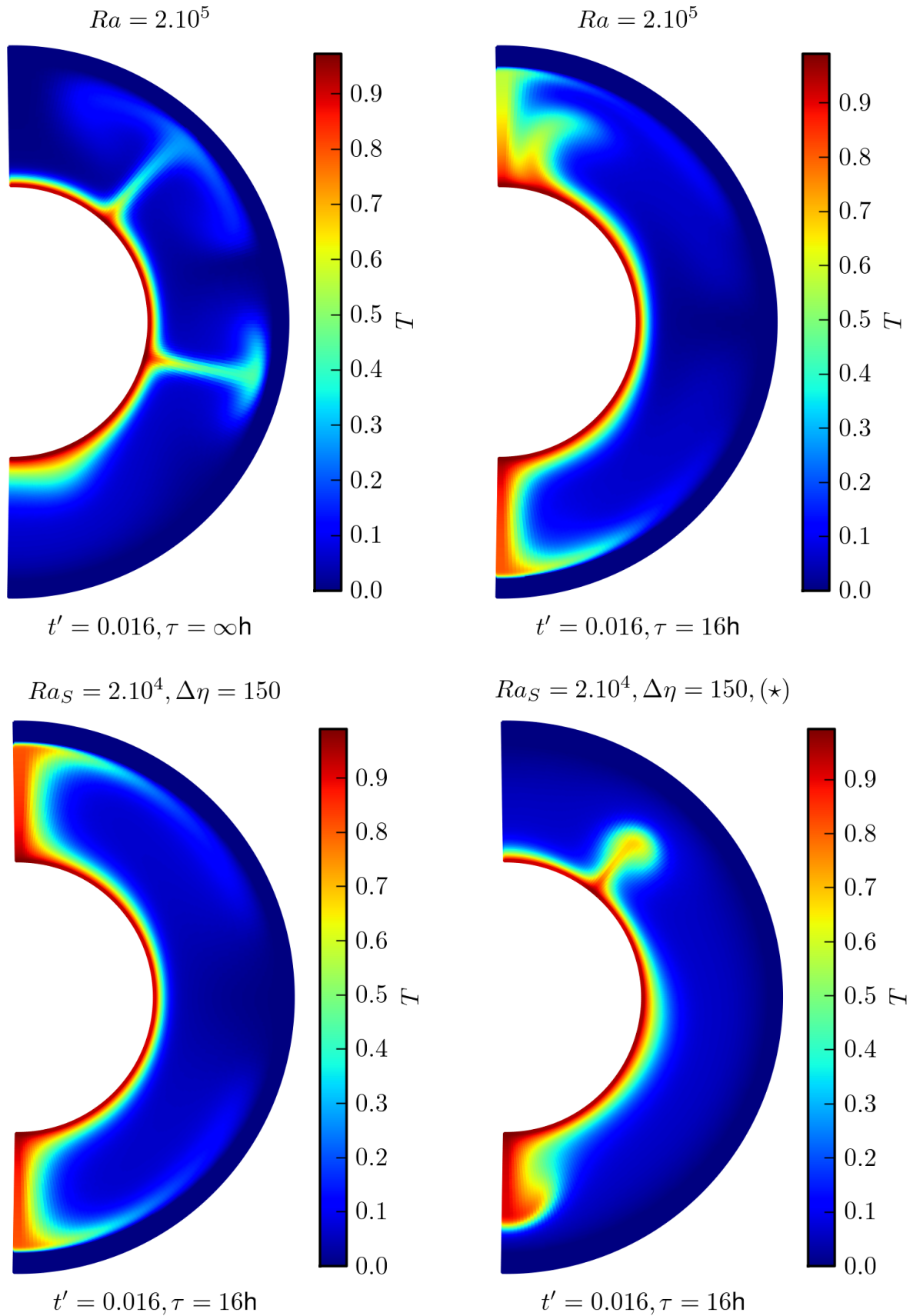
$t' = 0.016, \tau = 16\mathsf{h}$

Figure 5.8: Comparison of temperature fields at $t = 20\,\mathrm{Myr}$ for models I, II, III, IV started from asymmetric initial condition. Cold outer layer corresponds to air.
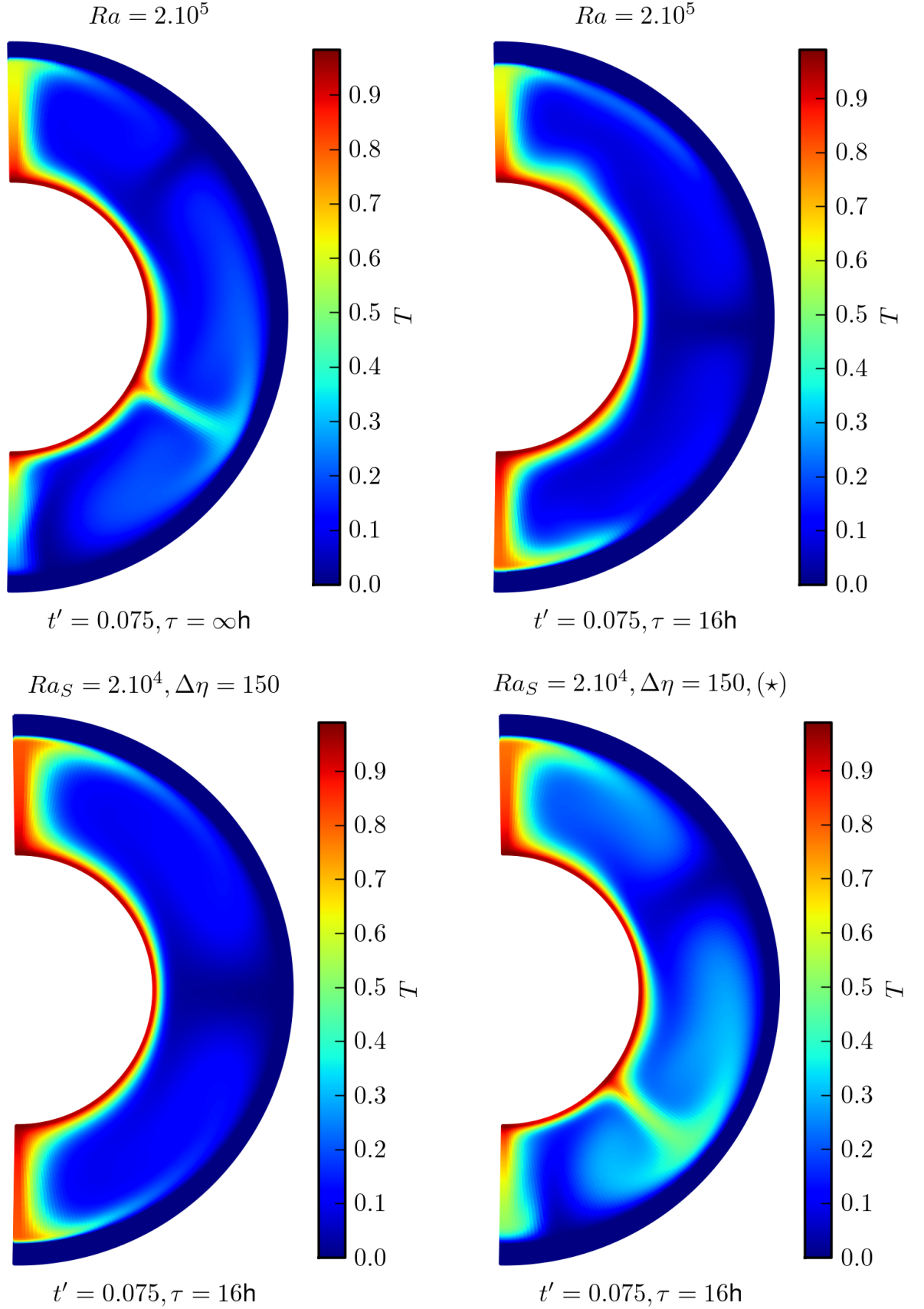
$$Ra = 2.10^5$$

$$t' = 0.075, \tau = \infty \mathsf{h}$$

$$Ra = 2.10^5$$

$$t' = 0.075, \tau = 16\mathsf{h}$$

$$Ra_S = 2.10^4, \Delta\eta = 150$$

$$t' = 0.075, \tau = 16\mathsf{h}$$

$$Ra_S = 2.10^4, \Delta\eta = 150, (\star)$$

$$t' = 0.075, \tau = 16\mathsf{h}$$

Figure 5.9: Comparison of temperature fields at $t = 95$ Myr for models I, II, III, IV started from asymmetric initial condition. Cold outer layer corresponds to air.
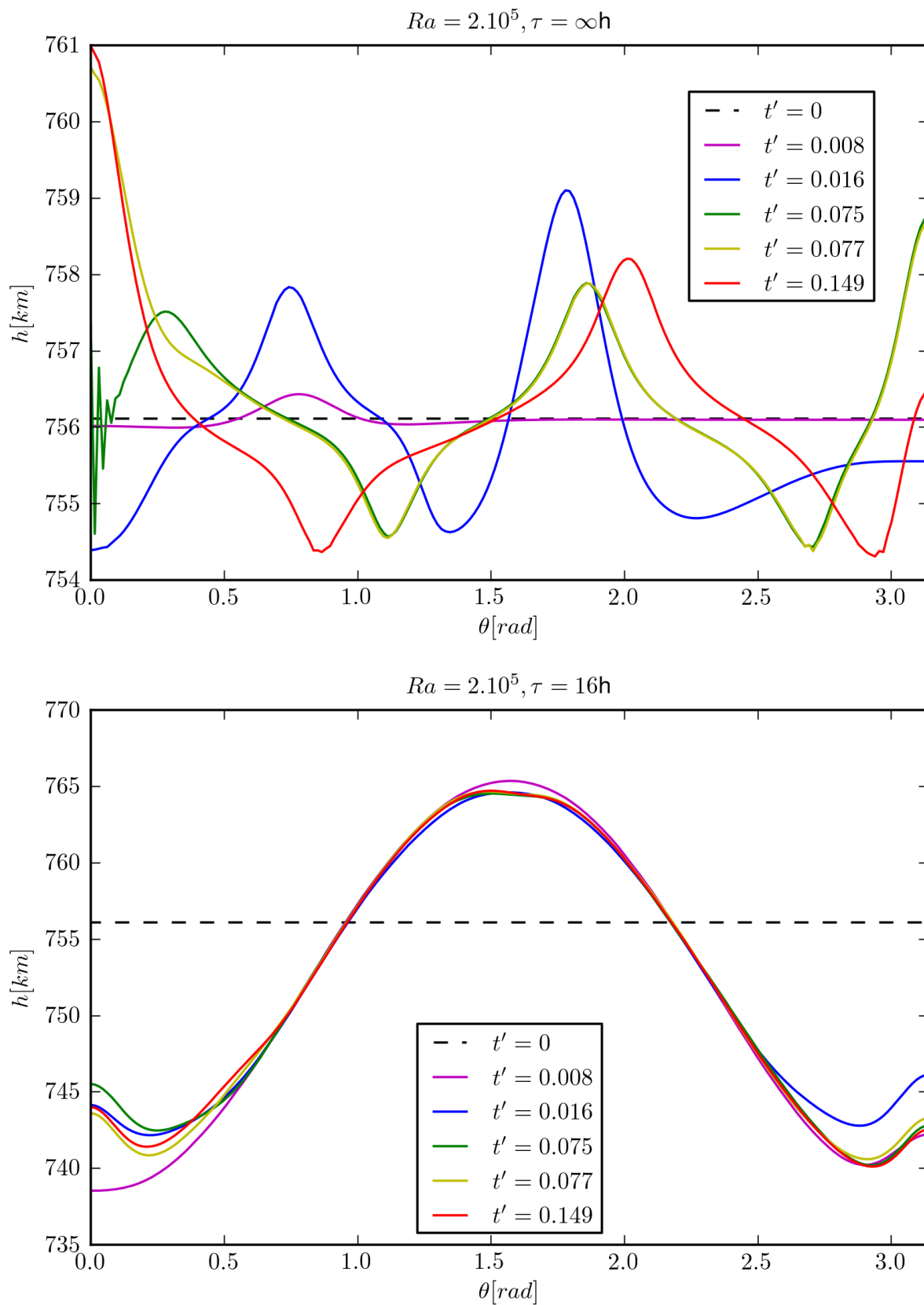
Figure 5.10: Surface evolution for model I and model II started from asymmetric initial condition. Snapshots of initial state and states at 10 Myr, 20 Myr, 95 Myr, 97 Myr and 190 Myr.
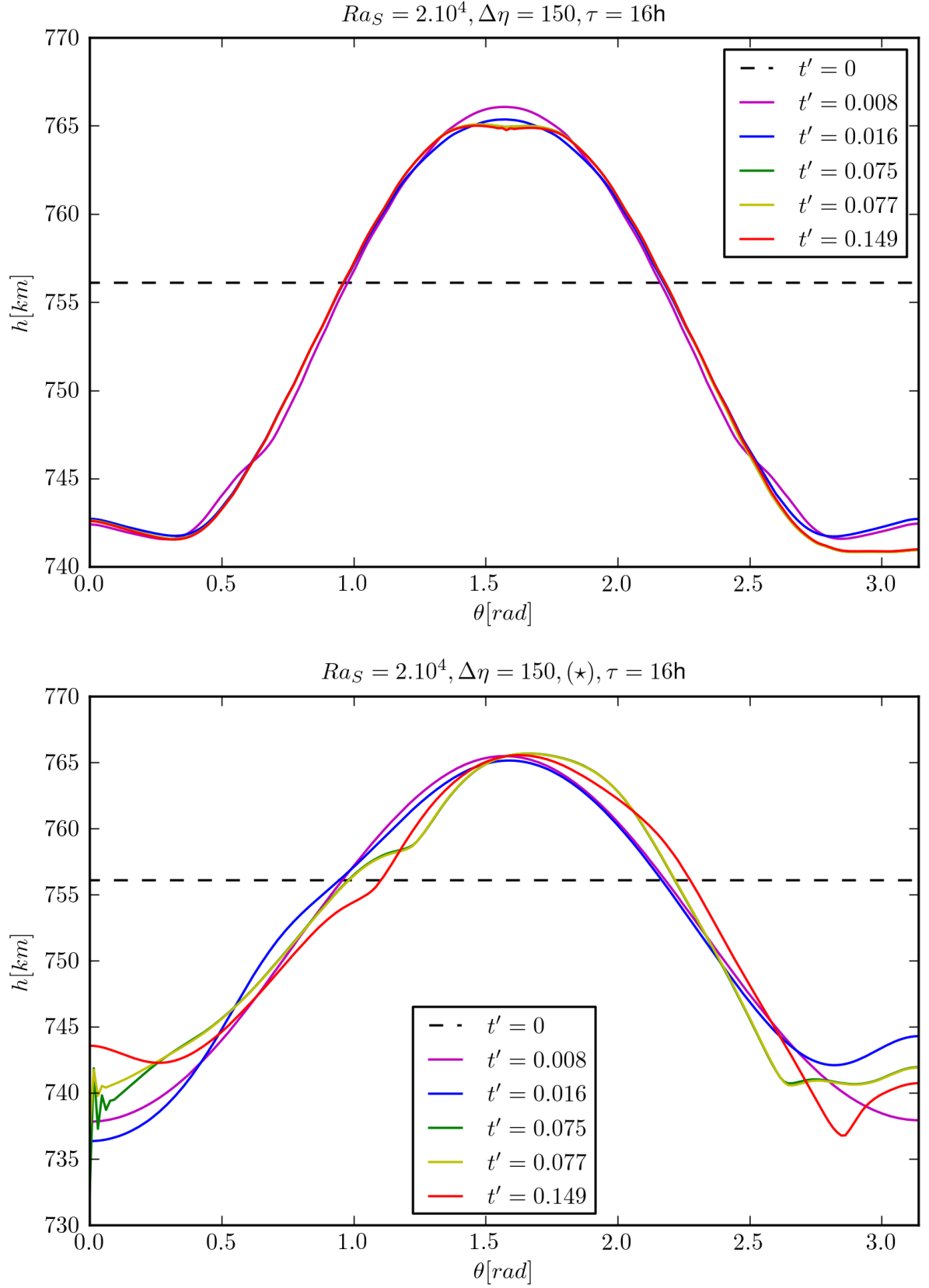
Figure 5.11: Surface evolution for model III and model VI started from asymmetric initial condition. Snapshots of initial state and states at 10 Myr, 20 Myr,95 Myr, 97 Myr and 190 Myr.

Conclusions

Having been motivated by presence of equatorial ridge on Iapetus whose origin is yet to be explained, we studied in this thesis thermal convection with free surface in a rotating icy satellite. In Chapter 1 we discussed the heat sources that warm the interior up so that convection can begin. We also discussed complicated nonlinear rheological properties of water ice. In Chapter 2 we introduced a simplified model that did not include nonlinear rheology but other than that was able to describe all the important phenomena related to the formation of ridge. The model was used for thorough tests of our numerical method. Governing equations of the model formed a stationary Stokes-Fourier system with temperature-dependent density that follows Boussinesq approximation, and temperature-dependent viscosity that follows Arrhenius law. Because of free surface, the equations were formulated on a time-dependent domain. In Chapter 3 we outlined the difficulties that free surface presents both to regularity theory and numerical methods. Having identified the main defects of our initial surface tracking method that was based on markers-at-cell method, we introduced our second approach, which uses surface-height method and variable density approximation. Numerical methods for solving Stokes problem, the heat equation and advection of surface were presented in Chapter 4. Using von Neumann stability analysis we proved unconditional stability of Crank-Nicolson and Implicit Upwind schemes for the heat equation. Using energy method we then proved unconditional stability of Implicit Upwind scheme for the advection equation. In Chapter 5 we subjected our numerical method to tests. The results of simulation of thermal convection in a solid spherical shell with $Ra = 2.10^5$ and $Ra = 2.10^6$ qualitatively agreed with the results in literature. The results of tests with free surface had reasonable physical interpretation.

Performance of our numerical method in these tests is encouraging. That said, method's ability to give quantitative predictions should be tested before the method is applied to model of Iapetus with internal heating, despinning and nonlinear rheology. Further, limits of the numerical method should be established. An obvious limitation of our surface tracking technique is its inability to handle surfaces that are multivalued with respect to θ. However, this limit should not be reached as the observations suggest only well-behaved deformations. Limits of the method that could be reached in simulations are due to variable density approximation. We hinted in Chapter 5 that turbulent flows in air could present difficulty. We also showed that smearing the viscosity discontinuity, which seems like a meaningful treatment, can affect the surface deformation. Regardless of the treatment, differences between the solutions of treated and untreated method should be quantified.

Based on the results of tests performed so far, we believe that our numerical method will help to explain the formation and the shape of Iapetian ridge. We also believe that it is a useful tool for numerical simulations of a broader class of problems with small deformations.

References

D. Breuer and W. B. Moore. Dynamics and Thermal History of the Terrestrial Planets, the Moon, and Io. In *Treatise on Geophysics*. Elsevier, 2007. 5, 6

M. Bulíček, P. Kaplický, and J. Málek. An L2-maximal regularity result for the evolutionary Stokes-Fourier system. *Applicable Analysis*, 90, 2011. 28

M. Běhounková. *Global and regional scale modeling of dynamic processes in the Earth's mantle*. PhD thesis, Charles University in Prague, 2007. 33

J. C. Castillo-Rogez, D. L. Matson, C. Sotin, T. V. Johnson, J. I. Lunine, and P. C. Thomas. Iapetus' geophysics: Rotation rate, shape, and equatorial ridge. *Icarus*, 190, 2007. 3, 6, 10, 13, 14, 16

J. C. Castillo-Rogez, T. V. Johnson, M. H. Lee, N. J. Turner, D. L. Matson, and J. I. Lunine. 26Al decay: Heat production and a revised age for Iapetus. *Icarus*, 204, 2009. 5

A. F. Cook and F. A. Franklin. An explanation of the light curve of Iapetus. *Icarus*, 13, 1970. 12

R. Dautray, J. L. Lions, C. Bardos, M. Cessenat, A. Kavenoky, I. N. Sneddon, P. Lascaux, B. Mercier, A. Craig, O. Pironneau, et al. *Mathematical analysis and numerical methods for science and technology: Evolution problems II*. Springer, 2000. 38, 39

W. B. Durham and L. A. Stern. Rheological properties of water ice - Applications to satellites of the outer planets. *Annual Review of Earth and Planetary Sciences*, 29, 2001. 7, 8, 9

E. Feireisl and A. Novotný. The Oberbeck-Boussinesq Approximation as a Singular Limit of the Full Navier-Stokes-Fourier System. *Journal of Mathematical Fluid Mechanics*, 11, 2009. 17

C. A. J. Fletcher. *Computational Techniques for Fluid Dynamics: Fundamental and general techniques*. Springer-Verlag, 1991. 35

T. V. Gerya. *Introduction to Numerical Geodynamic Modelling*. Cambridge University Press, 2010. 22

T. V. Gerya and D. A. Yuen. Characteristics-based marker-in-cell method with conservative finite-differences schemes for modeling geological flows with strongly variable transport properties. *Physics of The Earth and Planetary Interiors*, 140, 2003. 22

R. Greve. Fluid dynamics of planetary ices. *ArXiv e-prints*, March 2009. 7

D. Gross, W. Hauger, W. Schnell, and P. Wriggers. *Technische Mechanik: Band 4: Hydromechanik, Elemente Der Hoheren Mechanik, Numerische Methoden*. Springer, 2006. 10

C. W. Hirt and B. D. Nichols. Volume of fluid /VOF/ method for the dynamics of free boundaries. *Journal of Computational Physics*, 39, 1981. 20

H. Hussmann, C. Sotin, and J. I. Lunine. Interiors and Evolution of Icy Satellites. In *Treatise on Geophysics*. Elsevier, 2007. 4, 6

J. M. Hyman. Numerical methods for tracking interfaces. *Physica D: Nonlinear Phenomena*, 12, 1984. 25

M. Kuchta. Mantle flow modeling: application of a staggered grid method in a spherical geometry, 2008. 34

F. Maršík. *Termodynamika kontinua*. Academia, 1999. 26

S. McKee, M. F. Tomé, V. G. Ferreira, J. A. Cuminato, A. Castelo, F. S. Sousa, and N. Mangiavacchi. The MAC method. *Computers & Fluids*, 37, 2008. 21

D. Morrison, T. J. Jones, D. P. Cruikshank, and R. E. Murphy. The two faces of Iapetus. *Icarus*, 24, 1975. 12

J. Moser. *Mantle dynamics and rotation of the earth*. PhD thesis, Charles University in Prague, 1991. 41

K. Multhaup and T. Spohn. Stagnant lid convection in the mid-sized icy satellites of Saturn. *Icarus*, 186, 2007. 4

T. C. Owen, D. P. Cruikshank, C. M. Dalle Ore, T. R. Geballe, T. L. Roush, C. de Bergh, R. Meier, Y. J. Pendleton, and B. N. Khare. Decoding the Domino: The Dark Side of Iapetus. *Icarus*, 149, 2001. 12

S. J. Peale. Origin and evolution of the natural satellites. *Anual Review of Astronomy and Astrophysics*, 37, 1999. 6

Y. Ricard. Physics of Mantle Convection. In *Treatise on Geophysics*. Elsevier, 2007. 15, 16, 17

R. D. Richtmyer and K. W. Morton. *Difference methods for initial-value problems*. Interscience Publishers, 1967. 35, 36

G. Robuchon, G. Choblet, G. Tobie, O. Čadek, C. Sotin, and O. Grasset. Coupling of thermal evolution and despinning of early Iapetus. *Icarus*, 207, 2010. 3, 5, 6, 11, 13, 17

M. Segatz, T. Spohn, M. N. Ross, and G. Schubert. Tidal dissipation, surface heat flow, and figure of viscoelastic models of Io. *Icarus*, 75, 1988. 6

J. Serrin. On the interior regularity of weak solutions of the Navier-Stokes equations. *Archive for Rational Mechanics and Analysis*, 9, 1962. 28

T. Spohn and G. Schubert. Oceans in the icy Galilean satellites of Jupiter? *Icarus*, 161, 2003. 4

J. C. Strikwerda. *Finite difference schemes and partial differential equations*. Society for Industrial and Applied Mathematics, 2004. 35, 36

P. C. Thomas, J. A. Burns, P. Helfenstein, S. Squyres, J. Veverka, C. Porco, E. P. Turtle, A. McEwen, T. Denk, B. Giese, T. Roatsch, T. V. Johnson, and R. A. Jacobson. Shapes of the Saturnian icy satellites and their significance. *Icarus*, 190, 2007. 12, 13

W. R. van Schmus. Natural Radioactivity of the Crust and Mantle. In *Global Earth Physics: A Handbook of Physical Constants*. American Geophysical Union, 1995. 6

Appendix A

Balance Laws in Polar Coordinates

Continuity equation

$$\frac{1}{r^2}\frac{\partial(r^2 v_r)}{\partial r} + \frac{1}{r\sin\theta}\frac{\partial(\sin\theta v_\theta)}{\partial\theta} = 0$$

Momentum equation in direction $\vec{e}_r$

$$-\frac{\partial\pi}{\partial r} + \frac{1}{r^2}\frac{\partial(r^2\sigma_{rr})}{\partial r} + \frac{1}{r\sin\theta}\frac{\partial(\sin\theta\sigma_{r\theta})}{\partial\theta} + \frac{\sigma_{\theta\theta}}{r} + \rho f_r = 0$$

Momentum equation in direction $\vec{e}_\theta$

$$-\frac{1}{r}\frac{\partial\pi}{\partial\theta} + \frac{1}{r^2}\frac{\partial(r^2\sigma_{\theta r})}{\partial r} + \frac{1}{r\sin\theta}\frac{\partial(\sin\theta\sigma_{\theta\theta})}{\partial\theta} + \frac{\sigma_{\theta r}}{r} + \frac{\cot\theta}{r}\left(\sigma_{rr} + \sigma_{\theta\theta}\right) + \rho f_\theta = 0$$

Heat equation

$$\rho_{0,\text{ice}}C_p\left(\frac{\partial T}{\partial t} + v_r\frac{\partial T}{\partial r} + \frac{v_\theta}{r}\frac{\partial T}{\partial\theta}\right) = \frac{1}{r^2}\frac{\partial}{\partial r}\left(kr^2\frac{\partial T}{\partial r}\right) + \frac{1}{r^2\sin\theta}\frac{\partial}{\partial\theta}\left(k\sin\theta\frac{\partial T}{\partial\theta}\right)$$

Deviatoric part of stress tensor

$$\boldsymbol{\sigma} = \eta\left[\begin{array}{cc} 2\frac{\partial v_r}{\partial r} & \frac{1}{r}\left(\frac{\partial v_r}{\partial\theta} - v_\theta\right) + \frac{\partial v_\theta}{\partial r} \\ \frac{1}{r}\left(\frac{\partial v_r}{\partial\theta} - v_\theta\right) + \frac{\partial v_\theta}{\partial r} & \frac{2}{r}\left(\frac{\partial v_\theta}{\partial\theta} + v_r\right) \end{array}\right]$$

Appendix B

Finite Difference Approximations of Momentum Equation

Momentum equation in direction $\vec{e}_r$

The equation is differentiated in nodes $(i, j + 1)$. The difference equation takes the form $\vec{W}(i, j+1) \cdot \vec{V}(i, j+1) = (\rho f_r)(i, j+1)$, where $\vec{W}(i, j+1), \vec{V}(i, j+1) \in \mathbb{R}^{11}$ and f_r is radial component of the volume force. The vector of nodal values is defined as

$$\vec{V}(i, j+1) = \big(\pi_{(i-1,j+1)}, \pi_{(i+1,j+1)}, v_{r,(i-2,j+1)}, v_{r,(i+2,j+1)}, v_{r,(i,j+1)}, v_{r,(i,j+3)}, v_{r,(i,j-1)}$$
$$v_{\theta,(i-1,j+2)}, v_{\theta,(i+1,j+2)}, v_{\theta,(i-1,j)}, v_{\theta,(i+1,j)} \big). \tag{B.0.1}$$

Using notation $\vec{W}(i, j) = (W_1(i, j), W_2(i, j), \ldots, W_{11}(i, j))$, components of the vector of weights are then

$$W_1(i, j+1) = -\frac{1}{2\Delta r}, \tag{B.0.2}$$

$$W_2(i, j+1) = \frac{1}{2\Delta r}, \tag{B.0.3}$$

$$W_3(i, j+1) = \frac{\eta_{(i,j+1)}}{2 r_i \Delta r} + \frac{1}{r_i^2} \frac{r_{i-1}^2 \eta_{(i-1,j+1)}}{2 (\Delta r)^2}, \tag{B.0.4}$$

$$W_4(i, j+1) = -\frac{\eta_{(i,j+1)}}{2 r_i \Delta r} + \frac{1}{r_i^2} \frac{r_{i+1}^2 \eta_{(i+1,j+1)}}{2 (\Delta r)^2}, \tag{B.0.5}$$

$$W_6(i, j+1) = \frac{1}{r_i^2 \sin \theta_{j+1}} \frac{\sin \theta_{j+2} \eta_{(i,j+2)}}{4 (\Delta \theta)^2}, \tag{B.0.6}$$

$$W_5(i, j+1) = -\frac{1}{r_i^2} \frac{r_{i-1}^2 \eta_{(i-1,j+1)}}{2 (\Delta r)^2} - \frac{1}{r_i^2} \frac{r_{i+1}^2 \eta_{(i+1,j+1)}}{2 (\Delta r)^2}$$
$$- \frac{1}{r_i^2 \sin \theta_{j+1}} \frac{\sin \theta_{j+2} \eta_{(i,j+2)}}{4 (\Delta \theta)^2} - \frac{1}{r_i^2 \sin \theta_{j+1}} \frac{\sin \theta_j \eta_{(i,j)}}{4 (\Delta \theta)^2}, \tag{B.0.7}$$

$$W_7(i, j+1) = \frac{1}{r_i^2 \sin\theta_{j+1}} \frac{\sin\theta_j \eta_{(i,j)}}{4\left(\Delta\theta\right)^2}, \tag{B.0.8}$$

$$W_8(i, j+1) = \frac{\sin\theta_{j+2}\eta_{(i,j+2)}}{4r_i\Delta\theta \sin\theta_{j+1}} \left(\frac{1}{\Delta r} - \frac{1}{r_i}\right), \tag{B.0.9}$$

$$W_9(i, j+1) = \frac{\sin\theta_{j+2}\eta_{(i,j+2)}}{4r_i\Delta\theta \sin\theta_{j+1}} \left(-\frac{1}{\Delta r} - \frac{1}{r_i}\right), \tag{B.0.10}$$

$$W_{10}(i, j+1) = \frac{\sin\theta_j \eta_{(i,j)}}{4r_i\Delta\theta \sin\theta_{j+1}} \left(-\frac{1}{\Delta r} + \frac{1}{r_i}\right), \tag{B.0.11}$$

$$W_{11}(i, j+1) = \frac{\sin\theta_j \eta_{(i,j)}}{4r_i\Delta\theta \sin\theta_{j+1}} \left(\frac{1}{\Delta r} + \frac{1}{r_i}\right). \tag{B.0.12}$$

Momentum equation in direction $\vec{e}_\theta$

The equation is differentiated in nodes $(i+1, j)$. The difference equation takes the form $\vec{W}(i+1, j) \cdot \vec{V}(i+1, j) = (\rho f_\theta)(i+1, j)$ where $\vec{W}(i+1, j), \vec{V}(i+1, j) \in \mathbb{R}^{11}$ and f_θ is tangential component of the volume force. The vector of nodal values is defined as

$$\vec{V}(i+1, j) = \big(\pi_{(i+1,j+1)}, \pi_{(i+1,j-1)}, v_{\theta,(i-1,j)}, v_{\theta,(i+1,j)}, v_{\theta,(i+3,j)}, v_{\theta,(i+1,j+2)}, v_{\theta,(i+1,j-2)}$$
$$v_{r,(i,j+1)}, v_{r,(i,j-1)}, v_{r,(i+2,j+1)}, v_{r,(i+2,j-1)}\big). \tag{B.0.13}$$

Using notation $\vec{W}(i, j) = (W_1(i, j), W_2(i, j), \dots, W_{11}(i, j))$, components of the vector of weights are then

$$W_1(i+1, j) = -\frac{1}{2r_{i+1}\Delta\theta}, \tag{B.0.14}$$

$$W_2(i+1, j) = \frac{1}{2r_{i+1}\Delta\theta}, \tag{B.0.15}$$

$$W_3(i+1, j) = \frac{1}{r_{i+1}^2} \frac{r_i^2 \eta_{(i,j)}}{4\Delta r} \left(\frac{1}{\Delta r} - \frac{1}{r_i}\right) + \frac{\eta_{(i+1,j)}}{4r_{i+1}\Delta r}, \tag{B.0.16}$$

$$W_5(i+1, j) = -\frac{1}{r_{i+1}^2} \frac{r_{i+2}^2 \eta_{(i+2,j)}}{4\Delta r} \left(-\frac{1}{\Delta r} - \frac{1}{r_{i+2}}\right) - \frac{\eta_{(i+1,j)}}{4r_{i+1}\Delta r}, \tag{B.0.17}$$

$$
\begin{aligned}
W_4(i+1, j) = & \frac{1}{r_{i+1}^2} \frac{r_i^2 \eta_{(i,j)}}{4\Delta r} \left(-\frac{1}{\Delta r} - \frac{1}{r_i}\right) - \frac{1}{r_{i+1}^2} \frac{r_{i+2}^2 \eta_{(i+2,j)}}{4\Delta r} \left(\frac{1}{\Delta r} - \frac{1}{r_{i+2}}\right) \\
& - \frac{1}{r_{i+1}^2 \sin\theta_j} \frac{\sin\theta_{j+1}\eta_{(i+1,j+1)}}{2\left(\Delta\theta\right)^2} - \frac{1}{r_{i+1}^2 \sin\theta_j} \frac{\sin\theta_{j-1}\eta_{(i+1,j-1)}}{2\left(\Delta\theta\right)^2} \\
& - \frac{\eta_{(i+1,j)}}{r_{i+1}^2},
\end{aligned} \tag{B.0.18}
$$

$$W_6(i+1,j) = \frac{1}{r_{i+1}^2 \sin\theta_j} \frac{\sin\theta_{j+1}\eta_{(i+1,j+1)}}{2\left(\Delta\theta\right)^2} + \cot\theta_j \frac{\eta_{(i+1,j)}}{2\Delta\theta r_{i+1}^2}, \tag{B.0.19}$$

$$W_7(i+1,j) = \frac{1}{r_{i+1}^2 \sin\theta_j} \frac{\sin\theta_{j-1}\eta_{(i+1,j-1)}}{2\left(\Delta\theta\right)^2} - \cot\theta_j \frac{\eta_{(i+1,j)}}{2\Delta\theta r_{i+1}^2}, \tag{B.0.20}$$

$$W_8(i+1,j) = \frac{1}{r_{i+1}^2} \frac{r_i\eta_{(i,j)}}{4\Delta r\Delta\theta} + \frac{1}{r_{i+1}^2 \sin\theta_j} \frac{\sin\theta_{j+1}\eta_{(i+1,j+1)}}{2\Delta\theta}$$
$$+ \frac{\eta_{(i+1,j)}}{4r_{i+1}^2\Delta\theta} + \cot\theta_j \frac{\eta_{(i+1,j)}}{2r_{i+1}} \left(\frac{1}{r_{i+1}} + \frac{1}{\Delta r} \right), \tag{B.0.21}$$

$$W_9(i+1,j) = -\frac{1}{r_{i+1}^2} \frac{r_i\eta_{(i,j)}}{4\Delta r\Delta\theta} - \frac{1}{r_{i+1}^2 \sin\theta_j} \frac{\sin\theta_{j-1}\eta_{(i+1,j-1)}}{2\Delta\theta}$$
$$- \frac{\eta_{(i+1,j)}}{4r_{i+1}^2\Delta\theta} + \cot\theta_j \frac{\eta_{(i+1,j)}}{2r_{i+1}} \left(\frac{1}{r_{i+1}} + \frac{1}{\Delta r} \right), \tag{B.0.22}$$

$$W_{10}(i+1,j) = -\frac{1}{r_{i+1}^2} \frac{r_{i+2}\eta_{(i+2,j)}}{4\Delta r\Delta\theta} + \frac{1}{r_{i+1}^2 \sin\theta_j} \frac{\sin\theta_{j+1}\eta_{(i+1,j+1)}}{2\Delta\theta}$$
$$+ \frac{\eta_{(i+1,j)}}{4r_{i+1}^2\Delta\theta} + \cot\theta_j \frac{\eta_{(i+1,j)}}{2r_{i+1}} \left(\frac{1}{r_{i+1}} - \frac{1}{\Delta r} \right), \tag{B.0.23}$$

$$W_{11}(i+1,j) = \frac{1}{r_{i+1}^2} \frac{r_{i+2}\eta_{(i+2,j)}}{4\Delta r\Delta\theta} - \frac{1}{r_{i+1}^2 \sin\theta_j} \frac{\sin\theta_{j-1}\eta_{(i+1,j-1)}}{2\Delta\theta}$$
$$- \frac{\eta_{(i+1,j)}}{4r_{i+1}^2\Delta\theta} + \cot\theta_j \frac{\eta_{(i+1,j)}}{2r_{i+1}} \left(\frac{1}{r_{i+1}} - \frac{1}{\Delta r} \right). \tag{B.0.24}$$